



# Plastic strain recovery in nanocrystalline copper thin films

Nastaran Ghazi<sup>a,\*</sup>, Christian F. Niordson<sup>b</sup>, Jeffrey W. Kysar<sup>a</sup>

<sup>a</sup> Department of Mechanical Engineering, Columbia University, New York, NY 10027, USA

<sup>b</sup> Department of Mechanical Engineering, Solid Mechanics, Technical University of Denmark, Kgs. Lyngby, DK-2800, Denmark



## ARTICLE INFO

### Keywords:

Plastic strain recovery  
Grain boundaries  
Diffusion  
Finite element  
Voids

## ABSTRACT

Plastic strain recovery is a distinctive behavior of nanocrystalline thin film metals whereby plastic strain induced via application of an external load is gradually recovered over a time period of hours to days after load removal. Previous studies to model plastic strain recovery assumed that grain boundary sliding or grain boundary diffusion with heterogeneous diffusivity was the dominant deformation mechanism. In this study we propose that grain boundary diffusion in the presence of nanoscopic voids can lead to plastic strain recover without having to assume a sliding or heterogeneous diffusivity on grain boundaries. To model the system numerically in the context of the finite element method, we include a diffusion zone (DZ) and a cohesive zone (CS) on the grain boundaries and also include the possibility of plastic deformation in the surrounding grains. Our results suggest that diffusion leads to a mass flux toward the “void tips” (i.e. intersections of the voids and grain boundaries) as the external load is applied. Upon removal of the load, the additional material that accumulated near the void tips introduces a compressive residual normal stress on the grain boundary. The gradient of grain boundary residual stress leads to diffusion flux away from the void tip along the grain boundary in addition to diffusion flux to the void surface from the grain boundary. This redistribution of mass leads to a reduction in specimen length that is interpreted in terms of plastic strain recovery. With time the diffusion flux reduces the grain boundary stress gradient to the point where further grain boundary diffusion flux becomes negligible, after which diffusion flux occurs predominantly from the grain boundary at the void tip to the void surface. Since only one mass flux route remains active, the predicted plastic strain recovery rate is smaller. These simulation results are consistent with our experimental results that indicate plastic strain recovery exhibits two characteristic rates: a “fast” strain rate of about  $[10^{-7}] \text{ s}^{-1}$  followed by transition to a “slow” strain rate of about  $[10^{-9}] \text{ s}^{-1}$ .

## 1. Introduction

Nanocrystalline thin metal films with an average grain size less than  $[100] \text{ nm}$  have been the subject of widespread research in recent years due to their enhanced material properties and behavior compared to their coarse-grain counterparts. These material properties include higher yield strength, fracture strength, and strain rate sensitivity (Gleiter, 2000; Kumar et al., 2003a; Weertman, 2007). One of the unique properties of nanocrystalline thin film metals is a phenomenon called *plastic strain recovery*, where plastic strain introduced through a load cycle is gradually recovered (i.e. reversed) under no external loading over a time period of hours and days (Rajagopalan et al., 2007; WeiKysar, 2011; Ghazi and Kysar, 2016). However plastic strain recovery is not a reversible process in the thermodynamic sense because energy is dissipated during the load cycle. Along with the inverse Hall-Petch effect (Schiotz et al.,

\* Corresponding author.

E-mail address: [nng2107@columbia.edu](mailto:nng2107@columbia.edu) (N. Ghazi).

1998; Conrad and Narayan, 2000; Wolf et al., 2003), plastic strain recovery in nanocrystalline materials is a phenomenon that is counterintuitive to our understanding of inelastic deformation in microcrystalline materials and thus presents the opportunity to study the interactions between different deformation mechanisms at the nanometer length scale.

In microcrystalline materials, the dominant deformation mechanisms for plastic deformation are the creation, motion, and multiplication of dislocations. However when the grain size of the material is reduced to the nanometer scale, the small grain volumes constrain the activation of bulk dislocation sources, inhibiting dislocation-mediated plastic deformation, and making it possible for nanocrystalline metals to achieve significantly higher stresses than their microcrystalline counterparts. Given the high stresses coupled with the large volume fraction of grain boundaries in nanocrystalline metals, inelastic deformation in nanocrystalline metals is often dominated by grain boundary deformation mechanisms (Meyers et al., 2006; Hahn and Meyers, 2015) including grain boundary diffusion and grain boundary sliding (Swygenhoven and Derlet, 2001; Wei and Anand, 2004; Wei et al., 2008a). The inverse Hall-Petch effect and strain rate sensitivity (Wei et al., 2004, 2008b) observed in nanocrystalline metals—but not in microcrystalline metals—are also the result of grain boundary deformation mechanisms.

Plastic strain recovery occurs at very small rates ranging from  $10^{-9}$  s<sup>-1</sup> to  $10^{-7}$  s<sup>-1</sup> (Rajagopalan et al., 2007; Ghazi and Kysar, 2016; Wei et al., 2007) suggesting that grain boundary diffusive mechanisms play a key role in the phenomenon (WeiKysar, 2011; Wei et al., 2008b). A number of prior models suggest that plastic strain recovery is driven by residual stress in the film induced during loading. Several models propose that creep deformation due to residual stresses caused by grain size heterogeneity is responsible for recovery (Spolenak et al., 2001; Rajagopalan et al., 2008; Koslowski, 2010). Other models propose that the dominant deformation mechanism is the nucleation and activation of dislocations (Xie and Koslowski, 2016). Finally, others propose that grain boundary diffusion accommodated by sliding or plasticity inside the grains plays the key role in plastic strain recover (WeiKysar, 2011; Wei et al., 2008a; Li et al., 2009).

In this paper we propose a new mechanistic model for plastic strain recovery in nanocrystalline thin films based on the hypothesis that grain boundary diffusion is the dominant inelastic deformation mechanism that leads to recovery. The model accounts for the presence of grain boundaries interacting via diffusion with voids that exist within the nanocrystalline metal thin films due to the deposition process. A number of prior studies have observed that nanoscopic voids are commonly found in nanocrystalline materials (Meyers et al., 2006; Kumar et al., 2003b; Petegem et al., 2003; Hugo et al., 2003). Most of these studies described different deposition methods to fabricate nanocrystalline thin films, however the existence of voids can be justified for all thin films due to the presence of contaminants during deposition in the absence of absolute vacuum, as well as the existence of defects in substrates and impurities in substrate and thin film materials. Also, when film deposition proceeds via hit-and-stick mechanisms — such as the evaporation and sputtering methods that we used to fabricate our experimental samples — voids can result from self-shadowing effects during deposition. When the overall atomic mobility is low (specifically for sputtering where the substrate is low temperature), these voids can not be filled and remain in the thin films (Thornton and Hoffman, 1989; Koch, 2010). In addition voids can be nucleated during loading because of pre-existing defects in grain boundary or can be created by dislocation emission from grain boundaries (Kumar et al., 2003b; Meyers et al., 2006). Also the existence and growth of voids in nanocrystalline materials and its role in deformation behaviour has been demonstrated in number of recent numerical simulations (Dongare et al., 2009; Rudd, 2009; Bringa et al., 2010).

Our model allows for three possible irreversible deformation mechanisms: (1) diffusion along grain boundaries and along the surface of voids; (2) grain boundary fracture; and, (3) plastic deformation within the nanocrystalline grains. Numerically, grain boundary diffusion is modeled with a diffusion zone (DZ) model while potential fracture along grain boundaries is modeled by a cohesive zone (CZ) model. Continuum plastic deformation is treated as being isotropic. We purposely do not include the possibility of grain boundary sliding in order to test the hypothesis that grain boundary diffusion can be the dominant deformation mechanism associated with plastic strain recovery.

We employ the finite element method (FEM) to implement our model and validate it against our previously published (Ghazi and Kysar, 2016) experiments on plastic strain recovery in free-standing thin films of nanocrystalline copper. The diffusion zone (DZ) and cohesive zone (CZ) deformation mechanisms and their constitutive relationships are implemented through a user element (UEL) subroutine in the commercial finite element code ABAQUS. Our results are consistent with our previous experimental studies (Ghazi and Kysar, 2016) and suggest that grain boundary diffusion in conjunction with voids within the nanocrystalline material can be the dominant deformation mechanisms that lead to plastic strain recovery.

In what follows, Section 2 discusses previous experiments that characterize plastic strain recovery. Section 3 includes a description of the geometry of the specimen configuration investigated in this study as well as a description of the general computational methods used to model plastic strain recovery in the specimen. Section 4 describes the constitutive models used to model cohesive zone and diffusion zone behavior on grain boundaries as well as the diffusion zone behavior on the void surface. Section 5 describes the implementation of the cohesive and diffusion zones in the context of the finite element method. Section 6 discusses the development of the computational model from the cohesive zone and diffusion zone elements. Section 7 discusses the simulation results obtained throughout a load cycle followed by a recovery period during which plastic strain recovery emerges naturally from the simulation. Section 8 discusses the influence of model parameters on the simulation results. Section 9 summarizes results and presents conclusions.

## 2. Prior studies of plastic strain recovery

### 2.1. Prior experiments

The phenomenon of plastic strain recovery was first reported by (Rajagopalan et al., 2007) in nanocrystalline thin films of aluminum and gold. The microscale specimens were loaded uniaxially at strain rates in the range of  $10^{-4} \text{ s}^{-1}$  to plastic strains of the order of 0.65%. After load removal, the plastic strain was fully to partially recovered. The strain recovery rate increased with temperature. Additional experiments by (WeiKysar, 2011) and (Ghazi and Kysar, 2016) characterized the response of free-standing thin films of nanocrystalline copper loaded in plane strain deformation via a thin film bulge test to a total plastic strain of about 0.5%. The results demonstrate that plastic strain recovery occurs in two phases. During the transient first phase, plastic strain recovery occurs at a rate of about  $10^{-7} \text{ s}^{-1}$  for about  $2 \times 10^3 \text{ s}$ . During the steady-state second phase, plastic strain recovery rate decreases to about  $10^{-9} \text{ s}^{-1}$  and maintains this rate until the specimen has recovered its original dimensions. The two characteristic plastic strain rates as well as the time at which the transition occurs from one strain rate to another serve as important validation quantities.

### 2.2. Prior simulation models

Atomistic modeling (e.g. Molecular Dynamics) and continuum modeling (e.g. Finite Element Modeling) have been used to analyze experimental observations in nanocrystalline materials. Each method has strengths and weaknesses. Atomistic simulations provide descriptions of nanocrystalline deformation (Schiotz et al., 1998; Van Swygenhoven et al., 2002; Wolf et al., 2005; Swygenhoven et al., 2006) characterized in terms of grain boundary-mediated and dislocation-mediated deformation modes (Swygenhoven and Derlet, 2001; Swygenhoven et al., 2006; Swygenhoven and Weertman, 2006). The advantage of the atomistic method is that it directly models the atoms and therefore incorporates the atomic length scales of the grain boundary into the computation. Individual atoms interact through forces defined by potential functions. These potential functions are phenomenological approximations which in principle may be derived from quantum mechanical simulations. The primary drawback of atomistic-scale analysis is the time scale used in the simulations. In practice, the time step is a small fraction of the period of atomic vibration resulting in molecular dynamic calculations occurring at extremely high strain rates that are inaccessible experimentally. Another limitation of atomistic models is the accessible length scale. The largest sample that may be simulated typically on the order of only a few micrometers.

Finite element method (FEM) continuum simulations capture the mechanical response of nanocrystalline metals by modeling plastic deformation within individual grains as well as deformation mechanisms associated with the grain-boundary. While finite element methods have no limit for accessible length and time scales, the challenge is to model atomic scale phenomena at the continuum level (Meyers et al., 2006; Fu et al., 2001). In our study we address this issue by using continuum concepts to model atomic diffusion flux inside grain boundaries and over the void surfaces in the thin film while elastic-plastic deformation occurs within the grains simultaneously.

A limited number of studies have modeled plastic strain recovery phenomena. Wei and Anand (Wei et al., 2006) model inelastic deformation and failure in face-centered cubic (FCC) nanocrystalline metals using continuum modeling. In their model, grain boundary elements follow evolution equations for normal and tangential tractions across grain boundaries, and the grain interior follows single-crystal plasticity behavior. Their simulation results suggest a transition from “grain interior” to “grain boundary shearing” deformation as grain sizes decrease from 50 nm to 10 nm. Wei and Gao (Wei et al., 2008a) propose a grain boundary-mediated model with heterogeneous grain boundary diffusion and sliding able to reproduce plastic recovery observed in nanocrystalline aluminum thin films. In this study, the grain interior is assumed to deform by anisotropic elasticity with each grain boundary assigned either high or low values of diffusivity and sliding viscosity. Both these studies allow for grain boundary sliding. In the present study, we demonstrate that plastic strain recovery can be modeled by appealing to grain boundary diffusion with no grain boundary sliding. Importantly, our model captures the two characteristic plastic strain recovery rates as well as the transition between the two, which provides strong experimental validation.

## 3. Basic outline of mechanistic model

In our experimental setup (Ghazi and Kysar, 2016) a rectangular free-standing nanocrystalline copper thin film is deformed in

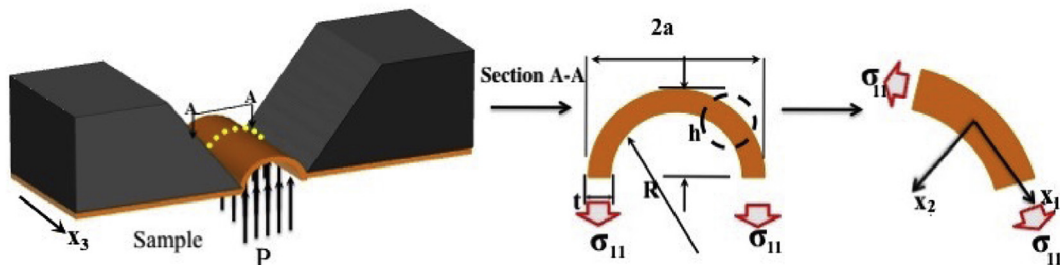


Fig. 1. Schematic of the sample representing the film in experimental condition.

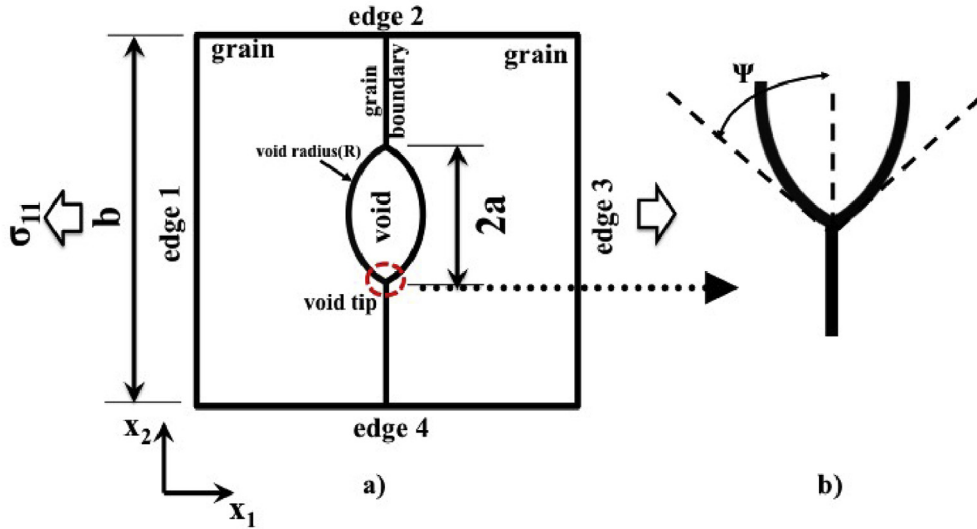


Fig. 2. a) Schematic of the model with periodic boundary conditions at edges 1 to 4 and pre-existing void between two grains, b) Dihedral angle ( $\psi$ ) at the tip of the void.

tension while maintaining a plane strain deformation state using a thin film bulge test (cf. Fig. 1). The film thickness is denoted by  $h$ , the length of the deforming film is denoted by  $2a$ , and the out-of-plane width is denoted by  $w$ . As air at a pressure,  $P$ , is applied uniformly across the film the specimen deforms into a cylindrical shape. The ratio  $h/a \ll 1$  so the film can be treated as a membrane. Furthermore the ratio  $w/a > 4$  so the deformation can be assumed to be plane strain (Vlassak and Nix, 1992; Xiang et al., 2006). To model the experiment, we select a 2D cross-section of the sample (Fig. 1) and assume a state of pure tension under a plane strain deformation state.

The thin metal film is treated as polycrystalline. For simplicity, all grains are considered to have similar shape and dimensions and we employ periodic boundary conditions (PBC) so our model reduces to a single unit cell that contains two grains separated by a grain boundary containing a single pre-existing void as shown in Fig. 2a. The void surface is approximated by two arcs with uniform radius, denoted as  $R$ , truncated by the grain-boundary at their points of intersection. The  $x_1$ -direction in Fig. 2a corresponds to the circumferential direction of the bulged specimen's mid-surface in Fig. 1. Similarly the  $x_2$ -direction corresponds to the radial direction of the bulged specimen, and the  $x_3$ -direction is in the longitudinal direction perpendicular to Section A-A (Fig. 1).

To impose PBC, the displacement in Fig. 1 is constrained to be zero in  $x_1$ -direction at edge 1 and in the  $x_2$ -direction at edge 4, with uniform displacement in the  $x_1$ -direction on edge 3 and in the  $x_2$ -direction on edge 2. All out-of-plane components of the strain tensor are assumed to be identically zero due to the plane strain conditions of the experimental setup. A uniform tensile stress,  $\sigma_{11}^\infty$ , is applied in the  $x_1$ -direction on edges 1 and 3. Since the pressure  $P \ll \sigma_{11}^\infty$ , we assume that edges 2 and 4 are free of tractions. The material within the grains is assumed to undergo isotropic elastic-plastic deformation.

Our model demonstrates that grain boundary diffusion is able to explain both the transient and steady-state plastic strain recovery rates. In contrast to earlier models for plastic strain recovery where heterogeneity in diffusion coefficient leads to atomic flux for recovery (Wei et al., 2008a), our model assumes a constant diffusion coefficient over all grain boundaries. Diffusion is driven by chemical potential gradients resulting from residual stresses and the presence of voids in the film.

To account for grain boundary diffusion, we incorporate a diffusion zone (DZ) associated with the grain boundary with initial thickness chosen arbitrarily to be 1 nm; its thickness can vary as a consequence of diffusion flux. A cohesive zone (CZ) is also associated with the grain boundary to account for potential traction-separation behavior. The system is assumed to be in mechanical equilibrium before application of an external force. A force balance equilibrium therefore holds at the tip of the void, implying that the surface tensions and grain boundary tension balance each other at the tip (Takahashi et al., 1991) such that

$$\gamma_b = 2\gamma_s \cos\psi \tag{1}$$

where  $\gamma_b$  denotes grain boundary energy per unit area,  $\gamma_s$  denotes surface energy per unit area, and  $\psi$  is the dihedral angle (cf. Fig. 2b). These surface energies are defined to be equal to the energy required to separate the adjoining surfaces if displacements jumps are normal to the grain boundary and surface and are prescribed to be  $\gamma_s \approx \gamma_b = 0.5 \text{ J/m}^2$  (Harper et al., 1999). With these values the dihedral angle at the tip is found to be

$$\psi = \arccos\left(\frac{\gamma_b}{2\gamma_s}\right) = 60^\circ. \tag{2}$$

The relation between the radius of the void,  $R$ , the void half-length  $a$ , and the dihedral angle is

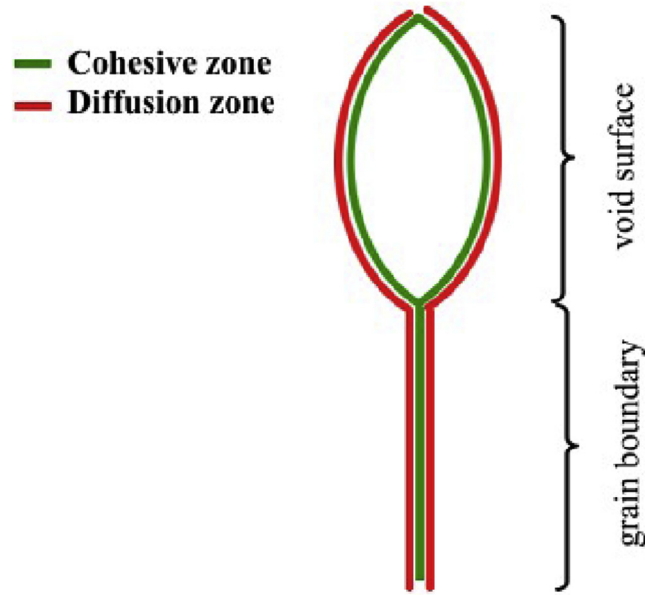


Fig. 3. Cohesive (green line) and diffusion (red line) zones over the grain boundary and pre-existing void. (For interpretation of the references to colour in this figure legend, the reader is referred to the Web version of this article.)

$$R = \frac{a}{\sin\psi}. \tag{3}$$

Our model implements both the cohesive zone and a diffusion zone as shown schematically in Fig. 3. The cohesive zone admits deformation via traction-separation constitutive behavior of the grain boundary defined by a potential function. The diffusion zone admits deformation by accounting for the driving forces of atomic diffusion over the grain boundary and void surface to determine the direction and magnitude of atomic flux within the grain boundary. The diffusion mechanism continues after removal of external stress from the sample which leads to a reversal of the direction of atomic flux, inducing plastic strain recovery.

#### 4. Grain boundary and void constitutive models

##### 4.1. Cohesive zone (CZ) modeling

Cohesive zone modeling is a common method for investigating fracture processes and decohesion at the prolongation of crack tips and at other geometrical discontinuities in a material. This approach is widely used because it avoids singularities at a crack tip. Cohesive zone modeling can be implemented in numerical analysis in the finite element method and the boundary element method (Prandtl, 1933; Barenblatt, 1959; Dugdale, 1960; Shet and Chandra, 2002). Hillerborg and later Needleman were the first to apply cohesive surface models to simulate fracture initiation and growth in the metal in the context of FEM (Peterson et al., 1976; Needleman, 1987, 1990). Later, Xu and Needleman proposed a cohesive zone model for both normal and tangential fracture modes (Xu and Needleman, 1993).

To model cohesive zones with the finite element method, a pair of cohesive surfaces is discretized using interface elements. These elements incorporate a nonlinear traction–separation law that constitutes the relationship between the opening separation and the cohesive zone traction at equilibrium with the stress fields of the surrounding body (cf. Fig. 4a). The relationship between traction and separation is obtained from the derivative of the potential function whose integral represents the fracture energy (Wei and Anand, 2004; Needleman, 1987). By increasing the interfacial separation to a critical value,  $\delta_c$ , the traction across the interface increases to a maximum value,  $T_{max}$ , after which further increase in the separation between surfaces leads to a decrease in traction. After sufficiently large separation, the traction between surface layers vanishes resulting in complete decohesion (Needleman, 1987). The maximum traction represents the material strength (Fig. 4b), with initial slope related to the elastic stiffness of the surrounding material.

In this work we use the Park–Paulino–Roesler (PPR) potential function (Park et al., 2009). This potential function characterizes different modes of fracture energies with varying cohesive strengths, and also describes various material softening behaviors that represent a wide range of failure responses. The PPR potential function is defined as

$$\Psi(\Delta n, \Delta t) = \min(\phi_n, \phi_t) + \left[ \Gamma_n \left( 1 - \frac{\Delta n}{\delta n} \right)^\alpha \left( \frac{m}{\alpha} + \frac{\Delta n}{\delta n} \right)^m + \langle \phi_n - \phi_t \rangle \right] \times \left[ \Gamma_t \left( 1 - \frac{|\Delta t|}{\delta t} \right)^\beta \left( \frac{n}{\beta} + \frac{|\Delta t|}{\delta t} \right)^n + \langle \phi_t - \phi_n \rangle \right] \tag{4}$$

where  $\langle . \rangle$  is the Macauley bracket, i.e.

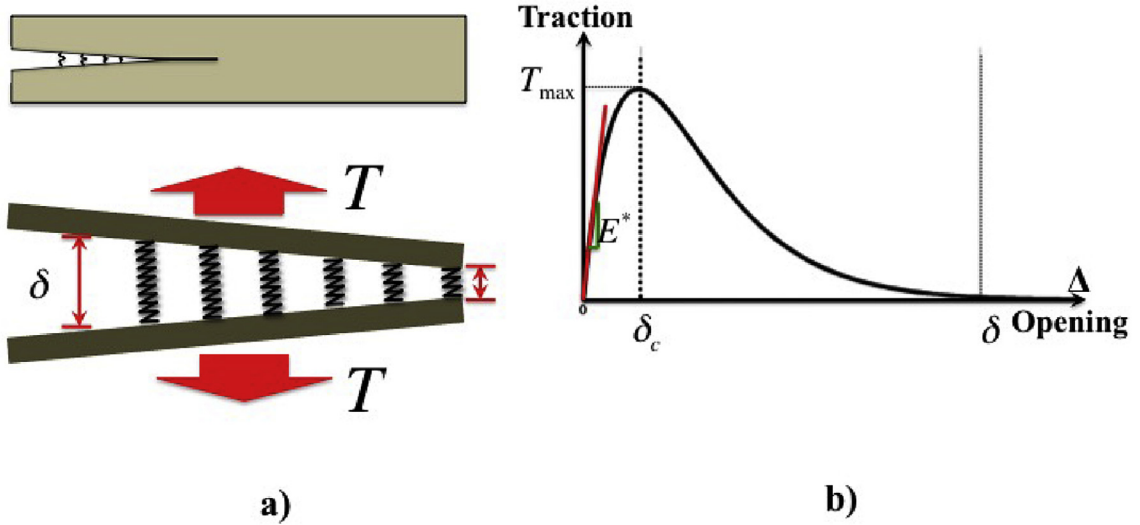


Fig. 4. General cohesive zone behavior: a) Two surfaces separating; b) Traction vs. Separation relationship.

$$\langle x \rangle = \begin{cases} 0, & (x \leq 0) \\ x, & (x > 0) \end{cases}$$

and where the parameters are defined based on expected material behavior in the regions of grain boundary and void tip. Table 1 defines each parameter in Eq. (4).

The first derivative of the potential with respect to crack openings provides tractions over the cohesive surface. In the case of the PPR potential

$$T_n(\Delta n, \Delta t) = \frac{\Gamma_n}{\delta n} \left[ m \left( 1 - \frac{\Delta n}{\delta n} \right)^\alpha \left( \frac{m}{\alpha} + \frac{\Delta n}{\delta n} \right)^{m-1} - \alpha \left( 1 - \frac{\Delta n}{\delta n} \right)^{\alpha-1} \left( \frac{m}{\alpha} + \frac{\Delta n}{\delta n} \right)^m \right] \times \left[ \Gamma_t \left( 1 - \frac{|\Delta t|}{\delta t} \right)^\beta \left( \frac{n}{\beta} + \frac{|\Delta t|}{\delta t} \right)^n + \langle \phi_t - \phi_n \rangle \right] \tag{5}$$

$$T_t(\Delta n, \Delta t) = \frac{\Gamma_t}{\delta t} \left[ n \left( 1 - \frac{|\Delta t|}{\delta t} \right)^\beta \left( \frac{n}{\beta} + \frac{|\Delta t|}{\delta t} \right)^{n-1} - \beta \left( 1 - \frac{|\Delta t|}{\delta t} \right)^{\beta-1} \left( \frac{n}{\beta} + \frac{|\Delta t|}{\delta t} \right)^n \right] \times \left[ \Gamma_n \left( 1 - \frac{|\Delta n|}{\delta n} \right)^\beta \left( \frac{n}{\beta} + \frac{|\Delta n|}{\delta n} \right)^n + \langle \phi_n - \phi_t \rangle \right] \times \frac{\Delta t}{|\Delta t|} \tag{6}$$

where  $T_n$  is normal traction and  $T_t$  is tangential traction. The values for the parameters in Table 1 are calculated using copper's atomic and macroscopic properties (cf. Table 2).

Fig. 5 shows the normal traction-separation relation curve obtained by applying the parameters to the cohesive zone relations in Eq. (5) and Eq. (6).

#### 4.2. Diffusion Zone (DZ) modeling

The concept of chemical potential (Gibbs, 1902) is defined as the increase in free energy when an individual atom is added into a system while the surface remains homogenous before and after adding the atom. Using the Gibbs energy definition, the chemical potential along the grain boundary is denoted as  $\mu_b$  and given as (Herring and Kingston, 1951)

$$\mu_{gb} = \mu_0 - \Omega \sigma_n \tag{7}$$

where  $\sigma_n$  denotes normal traction at position  $s$  on the grain boundary,  $\Omega$  is atomic volume, and  $\mu_0$  is a reference potential in the stress-

**Table 1**  
Cohesive zone parameters in the potential function based on PPR model.

|                            |                                      |
|----------------------------|--------------------------------------|
| $\phi_n, \phi_t$           | Mode I and Mode II fracture energy   |
| $\Gamma_n, \Gamma_t$       | Energy constants                     |
| $m, n$                     | Nondimensional exponents             |
| $\Delta_n, \Delta_t$       | Normal and Tangential Crack openings |
| $\delta_n, \delta_t$       | Final crack openings                 |
| $\delta_{nc}, \delta_{tc}$ | Critical crack openings              |
| $\alpha, \beta$            | Shape parameters                     |

**Table 2**  
Values of parameters employed in PPR potential function.

|  |  |
|--|--|
| $\alpha, \beta$  | 5,5  |
| $\delta_{nc}, \delta_{ic}$                                   | $8 \times 10^{-7}$ mm                      |
| $\frac{\delta_{nc}}{\delta_n}, \frac{\delta_{ic}}{\delta_n}$ | $\frac{1}{3}, \frac{1}{3}$                 |
| $\psi_{\text{grain boundary}}$                               | 0.5 J/m <sup>2</sup> (Harper et al., 1999) |
| $\psi_{\text{void surface}}$                                 | 0.5 J/m <sup>2</sup> (Harper et al., 1999) |

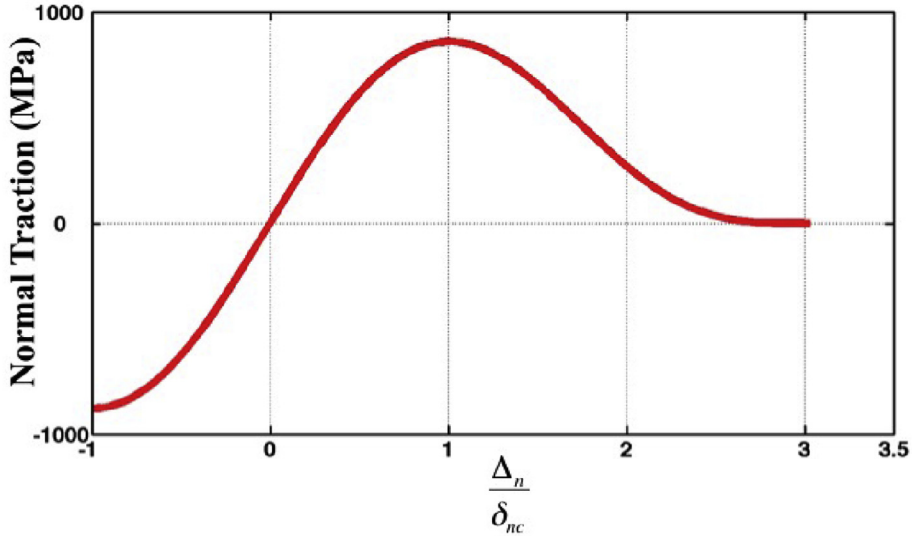


Fig. 5. Traction-Separation relation curve obtained using the values for variable in Table 2.

free state.

Atomic diffusion in the grain boundary is driven by the gradient of a non-uniform chemical potential along the boundaries. It is defined as the number of atoms per second which passes the grain boundary cross-section. The Nernst-Einstein equation for the atomic flux  $j_b$  is (Thouless, 1993)

$$j_{gb} = -\frac{\delta_{gb} D_{gb}}{kT\Omega} \frac{\partial \mu_{gb}}{\partial s} = \frac{\delta_{gb} D_{gb}}{kT} \left( \frac{\partial \sigma_n}{\partial s} \right) \tag{8}$$

where  $D_{gb}$  denotes the grain boundary diffusivity,  $\delta_{gb}$  is the grain boundary thickness,  $k$  is the Boltzmann constant,  $T$  is temperature, and  $s$  is position along the grain boundary.

Conservation of mass at the grain boundary requires that the rate of material accumulation at any point on the grain boundary is directly related to divergence of the atomic flux over the same point (cf. Fig. (6)), expressed as

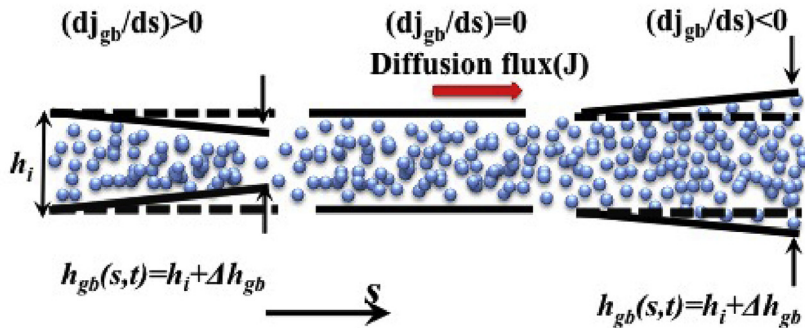


Fig. 6. Atomic diffusion flux in grain boundary shown as  $j_{gb}$  and  $h_i$  represents the initial thickness of the grain boundary whereas  $\Delta h_b$  represents the change in grain boundary thickness.

$$\Delta h_{gb} = -\Delta t \Omega \frac{\partial j_{gb}}{\partial s} \Rightarrow \dot{h}_{gb} = \frac{\Delta h_{gb}}{\Delta t} = -\frac{\partial(\Omega j_{gb})}{\partial s} = -\frac{D_{gb} \Omega}{kT} \frac{\partial}{\partial s} \left( h_{gb} \frac{\partial \sigma^n}{\partial s} \right) \quad (9)$$

where  $\Delta h_b$  represents normal displacement along the grain boundary.

#### 4.3. Constitutive model for diffusion on void surface

Surface diffusion is also driven by the variation in chemical potential along a free surface causing atoms to migrate from regions of high chemical potential to regions of low chemical potential. There are two contributions to the chemical potential ( $\mu_s$ ) from an atom on a free surface. The first is due to the surface free energy,  $\gamma_s$ , while the second is due to the elastic strain energy stored in the volume of material associated with an atom (LcBower et al., 1997). Thus the chemical potential on a free surface can be written

$$\mu_s = \mu_0 + \Omega(\phi - \gamma_s \kappa) \quad (10)$$

where  $\phi = \frac{1}{2} \sigma_{ij} \epsilon_{ij}$  is the elastic strain energy density (assuming a linear elastic material) and  $\kappa$  is the curvature of the surface. The sign convention for  $\kappa$  is that a concave surface has positive curvature and a convex surface has negative curvature. We assume that the rate of mass transport is proportional to the gradient in chemical potential. Therefore, the total flux on a void surface may be expressed as (Thouless, 1993)

$$j_s = -\mathcal{D}_s \left( \frac{\partial \mu_s}{\partial s} \right) \quad (11)$$

where  $s$  denotes the position measured from a convenient point on the void surface, and  $j_s$  is the volume of material that crosses a line of unit length perpendicular to the void's plane per unit time. The quantity  $\partial \mu_s / \partial s$  denotes the gradient in chemical potential along the void surface, and  $\mathcal{D}_s$  is a temperature dependent constant or proportionality related to the coefficient of surface diffusion (LcBower et al., 1997) by

$$\mathcal{D}_s = \frac{D_s \delta_s}{kT} e^{-\frac{Q_s}{kT}} \quad (12)$$

where the quantity  $D_s e^{-Q_s/kT}$  is the surface diffusion coefficient,  $\delta_s$  is the thickness of the diffusion layer calculated as the cubic root of the volume of the diffusive atom, and  $Q_s$  is the activation energy for surface diffusion.

The rate at which material is deposited on or removed from an element is related to the divergence of the surface flux by mass conservation. The normal velocity of the surface of the void in the reference configuration is

$$v_n = -\frac{\partial j_s}{\partial s}. \quad (13)$$

Upon rewriting Eq. (11) and Eq. (13) using Eq. (10) there results

$$j_s = -\mathcal{D}_s \left( \Omega \frac{\partial \phi}{\partial s} - \gamma_s \Omega \frac{\partial \kappa}{\partial s} \right) \quad (14)$$

and

$$v_n = \mathcal{D}_s \left( \Omega \frac{\partial^2 \phi}{\partial s^2} - \gamma_s \Omega \frac{\partial^2 \kappa}{\partial s^2} \right). \quad (15)$$

Deformation induced by the mechanical loading can be described by the displacement field  $u_i(x_j)$  of the material points from the stress free configuration of the solid. The deformation may be characterized by the infinitesimal strain

$$\epsilon_{ij} = \frac{1}{2} (u_{i,j} + u_{j,i}) \quad (16)$$

where the comma denotes partial differentiation with respect to the spatial coordinate. We assume that the solid deforms in the state of plane strain, with displacement components  $u_1 = u_1(x_1, x_2)$ ,  $u_2 = u_2(x_1, x_2)$  and  $u_3(x_1, x_2) = 0$ .

There is a discrete change in the magnitude of chemical potential at the point where the grain boundary meets the void surface. We refer to this position as the void tip and model the diffusion flux there as

$$J_{\text{void tip}} = -C(\mu_s - \mu_{gb}) \quad (17)$$

where  $C$  is a constant. A positive value of  $J_{\text{void tip}}$  represents the atomic flux from grain boundary to the grain boundary at the void tip.

## 5. Finite element implementation

We implemented the cohesive zone and diffusion zone as a User Element Subroutine (UEL) using Abaqus/Standard, which is a commercial finite element platform. Abaqus/Standard uses the Newton-Raphson method to model nonlinear equilibrium equations (Dassault Systèmes and Provid, 2013) based on the idea of linear approximation. This method is a rapidly converging process for solutions to problems where only one evaluation of the function is made at a time (Zienkiewicz and Taylor, 2005; Stroud, 2003).

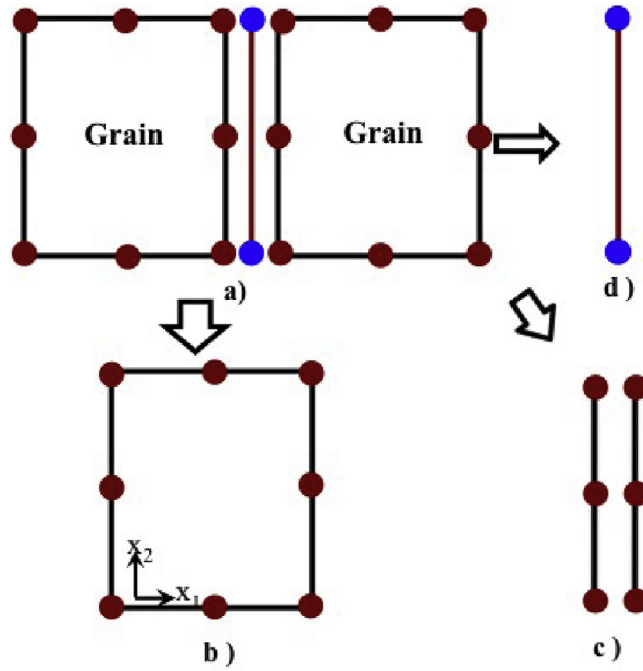


Fig. 7. Method to combine Cohesive Zone (CZ) element and Diffusion Zone (DZ) element between plane strain elements: a) Combination of elements in the model; b) Element inside the grain; c) Cohesive zone element; d) Diffusion zone element.

We first define the stiffness and residual matrix for each type of element. Using the Newton-Raphson method, the nonlinear relation between the field variables in the vector element  $\mathbf{u}$  (element opening displacement for cohesive zone element and atomic flux for diffusion zone element) and external force  $\mathbf{f}$  (traction for cohesive zone element and chemical potential for diffusion zone element) is defined as

$$K(\mathbf{u}) \times \mathbf{u} = \mathbf{f} \tag{18}$$

where  $K(u)$  is defined to be the stiffness matrix. For a nonlinear equation, the residual vector  $\mathbf{r}(\mathbf{u})$  is defined as

$$\mathbf{r}(\mathbf{u}) = K(\mathbf{u}) \times \mathbf{u} - \mathbf{f} \tag{19}$$

The basic formulation used to find the iterative correction for Newton's method is obtained as follows (Zienkiewicz and Taylor, 2005)

- (1)  $\mathbf{u}_{k+1} = \mathbf{u}_k$
- (2)  $\mathbf{r}_k = K(\mathbf{u}_k)\mathbf{u}_k - \mathbf{f}$
- (3)  $T(\mathbf{u}_k) \cdot \Delta \mathbf{u}_k = -\mathbf{r}_k \rightarrow \Delta \mathbf{u}_k = T^{-1}(\mathbf{u}_k) \cdot (-\mathbf{r}_k)$
- (4)  $\mathbf{u}_{k+1} = \mathbf{u}_k + \Delta \mathbf{u}_k$ .

5.1. Weak form and discretization for cohesive zone element

To discretize the domain inside the grain, a standard plane strain 8-node bi-quadratic element from the Abaqus element library (CPE8R) is chosen (Fig. 7a). The cohesive zone element between two grains is shown in Fig. 7b and Fig. (8). These elements are defined by a 6-node one-dimensional element integrated using three Gauss points. The shape function for the element is defined to be quadratic Lagrangian, preserving continuity of the field variable but not of its derivatives ( $C^0$ ). The field variables for the cohesive

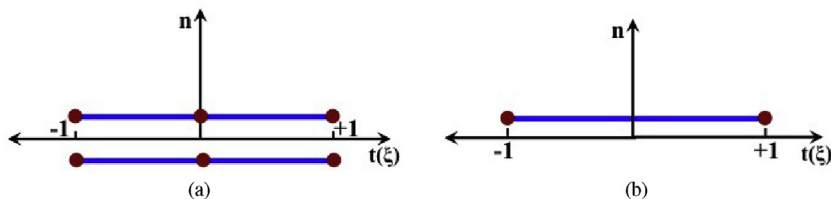


Fig. 8. Local coordinate systems: a) Cohesive zone element and nodes; b) diffusion zone element and nodes.

zone are defined as  $u^1$  and  $u^2$  in local  $x_1$ - and  $x_2$ -directions, respectively.

The projection of the displacement components in normal and tangential direction to the grain boundary is obtained as

$$u^n = \sum_{k=1}^{(2 \times 6)} (n_i Q_{ik}) U_k \tag{21}$$

$$u^t = \sum_{k=1}^{(2 \times 6)} (t_i Q_{ik}) U_k \tag{22}$$

where  $n_i$  is the normal vector to the cohesive interface and  $U_k$  is the displacement vector at element nodes. The matrix  $Q$  which represents the sequence of shape functions at different points of the element is defined as (Fish and Belytschko, 2007)

$$Q = \begin{bmatrix} S_1 & 0 & S_2 & 0 & S_3 & 0 & -S_1 & 0 & -S_2 & 0 & -S_3 & 0 \\ 0 & S_1 & 0 & S_2 & 0 & S_3 & 0 & -S_1 & 0 & -S_2 & 0 & -S_3 \end{bmatrix} \tag{23}$$

The shape functions are defined as

$$S_1 = \frac{1}{2}(\xi^2 - \xi)$$

$$S_2 = \frac{1}{2}(\xi^2 + \xi)$$

$$S_3 = 1 - \xi^2$$

where  $\xi$  is a normalized coordinate in the direction of the element (Fig. 8-a).

To include the effect of cohesive energy on a surface, a term reflecting this energy should be embedded into the constitutive potential function of the system. When adjacent nodes in an element move relative to each other, this movement causes the element to open normally or tangentially. The virtual work of this process is

$$\int_s (T^n \delta u^n + T^t \delta u^t) ds \tag{24}$$

which represents the cohesive surface energy. This term considers the effect of normal ( $T^n$ ) and tangential ( $T^t$ ) traction on the corresponding cohesive surface.

$T^n$  and  $T^t$  are rearranged by defining cohesive stiffness terms  $a_n$  and  $a_t$  as

$$T^n = T^n(\Delta n, \Delta t) = a^n(\Delta n, \Delta t) \times \Delta n \tag{25}$$

$$T^t = T^t(\Delta n, \Delta t) = a^t(\Delta n, \Delta t) \times \Delta t \tag{26}$$

where  $\Delta n = (u^n - (h - h_0))$ ,  $\Delta t = (u^t - u^s)$ ,  $h$  is the current grain boundary thickness,  $h_0$  is the initial grain boundary thickness, and  $u^s$  is the relative displacement across the grain boundary. By substituting  $T^n$  and  $T^t$  into the Eq. (24), the contribution of the cohesive zone element to the principle virtual work is obtained as

$$\int (a^n u^n \delta u^n + a^t u^t \delta u^t) ds - \int (a^n (h - h_0) \delta u^n + a^t u^s \delta u^t) ds. \tag{27}$$

Using the discretized form of  $u^n$  and  $u^t$  from Eq. (53) and Eq. (22) we can rewrite Eq. (53) as

$$\int (a^n (n_i Q_{iL}) U_L (n_j Q_{jK}) \delta U_K + a^t (t_i Q_{iL}) U_L (t_j Q_{jK}) \delta U_K) ds - \int (a^n (h - h_0) (n_j Q_{jK}) \delta U_K + a^t (t_j Q_{jK}) \delta U_K) ds \tag{28}$$

where summation over the lower indices  $K$  and  $L$  is implied. Thus Eq. (28) has the final form

$$K_{KL} U_L - f_K \tag{29}$$

where the matrix  $K$  and the vector  $f$  are

$$K_{KL} = \int [a^n (n_j Q_{jK}) (n_i Q_{iL}) + a^t (t_j Q_{jK}) (t_i Q_{iL})] ds \tag{30}$$

$$f_k = \int [a^n (n_j Q_{jK}) (h - h_0) + a^t (t_j Q_{jK}) (u^s)] ds. \tag{31}$$

The tangential stiffness matrix ( $T$ ) is obtained by using the Newton-Raphson definition as

$$T_{kl} = K_{kl} + \sum \frac{\partial K_{km}}{\partial U_l} U_m - \frac{\partial f_k}{\partial U_l} \tag{32}$$

where  $K$  and  $f$  are found from Eqs. (30) and (31). As described in detail in the Appendix 1, upon calculating all terms in Eq. (32) the stiffness matrix can be expressed as

$$T_{kl} = \int (n_j Q_{jK}) \left( a^n (n_i Q_{iL}) + \left( \frac{\partial a^n}{\partial u^n} n_i Q_{iL} (u^n - (h - h_0)) \right) + \left( \frac{\partial a^n}{\partial u^n} t_i Q_{iL} (u^n - (h - h_0)) \right) \right) ds + (t_j Q_{jK}) \tag{33}$$

$$\begin{aligned} & \left( a^t (t_l Q_{ll}) + \left( \frac{\partial a^t}{\partial u^t} t_l Q_{ll} (u^t - (h - h_0)) \right) + \left( \frac{\partial a^n}{\partial u^n} t_l Q_{ll} (u^n - (h - h_0)) \right) \right) ds \\ & = \int (a^{NN} (n_j Q_{jk})(n_l Q_{ll}) + a^{NT} (n_j Q_{jk})(t_l Q_{ll}) + a^{TN} (t_j Q_{jk})(n_l Q_{ll}) + a^{TT} (t_j Q_{jk})(t_l Q_{ll})) \end{aligned} \tag{34}$$

where

$$a^{NN} = \left[ a^n + \frac{\partial a^n}{\partial u^n} (u^n - (h - h_0)) \right]$$

$$a^{NT} = \frac{\partial a^n}{\partial u^t} (u^n - (h - h_0))$$

$$a^{TN} = \frac{\partial a^t}{\partial u^n} (u^t - u^s)$$

$$a^{TT} = \left[ a^t + \frac{\partial a^t}{\partial u^t} (u^t - u^s) \right]$$

Additionally, the residual can be expressed as

$$\begin{aligned} n_k = & K_{kl} U_l - f_k = \\ & \int [a^n (n_j Q_{jk})(n_l Q_{ll}) U_l + a^t (t_j Q_{jk})(t_l Q_{ll}) U_l] ds \\ & \int [a^n (h - h_0)(n_j Q_{jk}) + a^t u^s (t_j Q_{jk})] ds = \\ & \int [a^n (n_j Q_{jk})(u^n - (h - h_0)) + a^t (t_j Q_{jk})(u^t - u^s)]. \end{aligned} \tag{35}$$

### 5.2. Weak form and discretization of grain boundary diffusion zone element

To find the stiffness matrix for the diffusion flux it is necessary to define the weak form of Eq. 8

$$\int_{S_\Gamma} \left( j_{gb} - h \mathcal{L}_{gb} \frac{\partial \sigma^n}{\partial s} \right) \delta j_{gb} ds = 0 \tag{36}$$

where  $\delta j_{gb}$  is a “kinematically” admissible atomic flux-field,  $h$  represents diffusion zone thickness,  $\delta_{gb}$ , therefore

$$\int_{S_\Gamma} j_{gb} \delta j_{gb} ds = \int_{S_\Gamma} \left( h \mathcal{L}_{gb} \frac{\partial \sigma^n}{\partial s} \right) \delta j_{gb} ds. \tag{37}$$

The detail for all steps of calculation is described in Appendix 2. Eq. (37) acan be expressed respectively as

$$\begin{aligned} & \left( \int_{S_\Gamma} \left( \delta j_{(gb)k} S_{kl} S_{mn} - \mathcal{L}_{gb} \alpha \Omega \sigma^n \Delta t \delta j_{(gb)k} \frac{\partial S_{kl}}{\partial \zeta} \frac{\partial S_{mn}}{\partial \zeta} \left( \frac{2}{l} \right)^2 - \mathcal{L}_{gb} \alpha \Omega \sigma^n \Delta t \delta j_{(gb)k} S_{kl} \frac{\partial^2 S_{mn}}{\partial \zeta^2} \left( \frac{2}{l} \right)^2 \right) d\zeta \left( \frac{l}{2} \right) \right) j_{(gb)n} \\ & = - \int \mathcal{L}_{gb} \Omega \sigma^n h_0 \delta j_{(gb)k} \frac{\partial S_{kl}}{\partial \zeta} d\zeta + \mathcal{L}_{gb} \Omega \sigma^n \frac{\partial h_0}{\partial \zeta} \delta j_{(gb)k} S_{kl} + [h \mathcal{L}_{gb} \sigma^n (S_{kl} \delta j_{(gb)k})]_{-}^{+} \end{aligned} \tag{38}$$

where  $\sigma^n$  is calculated from the cohesive traction-separation equation inside the grain boundary. Over each element,  $\sigma^n$  is determined as a function of traction on each element's node using linear shape function  $S$

$$\sigma^n = \sum_{K=1}^3 S_K \sigma_K.$$

Since the shape function is linear, the second derivative in Eq. (38) is zero,  $\frac{\partial^2 S}{\partial \zeta^2} = 0$ . By implementing the summation in the Eq. (38), the finite element form of the equation is obtained as

$$K_{kn} j_{(gb)n} = F_n \tag{39}$$

where

$$K_{kn} = \int_{S_\Gamma} \left( S_{kl} S_{mn} - \mathcal{L}_{gb} \alpha \Omega \sigma^n \frac{\partial S_{kl}}{\partial \zeta} \frac{\partial S_{mn}}{\partial \zeta} \left( \frac{2}{l} \right)^2 \right) d\zeta \left( \frac{l}{2} \right) \tag{40}$$

and

$$F_n = - \int \left( \mathcal{L}_{gb} \sigma^n h_0 \frac{\partial S_{kl}}{\partial \zeta} + \mathcal{L}_{gb} \sigma^n \frac{\partial h_0}{\partial \zeta} S_{kl} \right) d\zeta + [h \mathcal{L}_{gb} \sigma^n (S_{kl} \delta j_k)]_{-}^{+}.$$

### 5.3. Weak form and discretization of void surface diffusion zone element

The flux on the void surface  $j_s$  is calculated by enforcing Eq. (14) in its weak form

$$\int_{\Gamma} j_s \delta j_s ds = - \int_{\Gamma} \mathcal{D}_s \left( \frac{\partial \phi}{\partial s} - \gamma_s \frac{\partial \kappa}{\partial s} \right) \delta j_s ds = \int_{\Gamma} \mathcal{D}_s (\phi - \gamma_s \kappa) \frac{\partial \delta j_s}{\partial s} ds - [\mathcal{D}_s (\phi - \gamma_s \kappa) (\delta j_s)]_+^+ \quad (41)$$

where normal velocity over the surface,  $v_n$ , is then determined as the gradient of the surface diffusion flux.

To obtain the finite element equation from the discretized form, the linear Gaussian shape function is defined over the diffusion zone element of the void surface as

$$\begin{aligned} & \left( \int_{\text{SF}} \left( \delta J_k S_{kl} S_{mn} - \mathcal{D}_s \alpha \Omega^2 \gamma_s \Delta t \delta J_k \frac{\partial^3 S_{kl}}{\partial \zeta^3} \frac{\partial S_{mn}}{\partial \zeta} \left( \frac{2}{l} \right)^4 - \mathcal{D}_s \alpha \Omega \gamma_s \Delta t \delta J_k \kappa_0 \frac{\partial S_{kl}}{\partial \zeta} \frac{\partial S_{mn}}{\partial \zeta} \left( \frac{2}{l} \right)^2 \right) d\zeta \left( \frac{l}{2} \right) \right) \\ & = - \int \mathcal{D}_b \gamma_s \kappa_0 \Omega \delta J_k \frac{2}{l} \frac{\partial S_{kl}}{\partial \zeta} d\zeta + [\mathcal{D}_s \gamma_s \kappa_0 (S_{kl} \delta J_k)]_+^+ \end{aligned} \quad (42)$$

$$K_{kn} J_n = F_n \quad (43)$$

where

$$K_{kn} = \int_{\text{SF}} \left( S_{kl} S_{mn} - \mathcal{D}_s \alpha \Omega \gamma_s \Delta t \kappa_0 \frac{\partial S_{kl}}{\partial \zeta} \frac{\partial S_{mn}}{\partial \zeta} \left( \frac{2}{l} \right) \right) d\zeta \quad (44)$$

and

$$F_n = - \int \mathcal{D}_b \gamma_s \kappa_0 \Omega \delta J_k \frac{\partial S_{kl}}{\partial \zeta} d\zeta + [\mathcal{D}_s \gamma_s \kappa_0 (S_{kl} \delta J_k)]_+^+.$$

The calculations is described in detail in Appendix 3.

## 6. Model development

### 6.1. Length scale limitations

The size effect for parameters in the constitutive equations of the cohesive zone and diffusion affect the final result of the simulation. It is therefore necessary to consider the length scales for each parameters. The most important parameters includes grain size,  $b$ , mesh size, and cohesive zone decohesion length. In this work, the Griffith model is used as a standard model that incorporates all of these parameters as a means to determine necessary relationships between length scales in the problem.

The stress intensity factor associated with periodically spaced Griffith cracks is (Kanninen and Popelar, 1985)

$$K_I = \sigma^\infty (\pi a)^{\frac{1}{2}} \left[ \frac{2b}{\pi a} \tan \left( \frac{\pi a}{2b} \right) \right]^{\frac{1}{2}} \quad (45)$$

where  $\sigma^\infty$  denotes the far-field stress and  $2a$  and  $b$  are the length of the void and the grain, respectively (cf. 9). While the Griffith cracks have a higher stress concentration than the voids used in the problem, they provide a lower bound on the stress,  $\sigma^\infty$ , required to achieve grain boundary fracture. The plane strain Griffith model relates Young's modulus,  $E$ , Poisson ratio,  $\nu$ , surface free energy,  $\gamma_s$ , and energy release rate,  $G$ , as (Kanninen and Popelar, 1985)

$$G = \frac{(1 - \nu^2)}{E} K_I^2 \quad (46)$$

where in the absence of inelastic deformation the grain boundary fracture criterion is  $G = 2\gamma_s$  (where we neglect the grain boundary free energy). The values for these material properties in our simulation using copper are  $G = [1] \text{ J/m}^2$ ,  $E = [150] \text{ GPa}$  and  $\nu = 0.3$  (Harper et al., 1999) whereby  $K_I = [0.406] \text{ MPa}\sqrt{\text{m}}$ . The minimum fair-field stress that could induce grain boundary fracture is

$$\sigma^\infty = K_I (\pi a)^{-\frac{1}{2}} \left[ \frac{2b}{\pi a} \tan \left( \frac{\pi a}{2b} \right) \right]^{\frac{1}{2}}. \quad (47)$$

The magnitude of the lower bound on far-field stress from Eq. (47) can be compared to the far-field stress obtained from simulations of different length parameters to explore the size effect.

In the finite element analysis of the cohesive zone, determining the appropriate mesh size is a critical issue related to the accuracy and computational efficiency. To find an adequate mesh size bound, we checked for mesh dependency of the Griffith model. We then validate the far-field stress obtained from the simulation by comparing them to Eq. (47) for different ratios of mesh size to critical opening at cohesive traction-separation relation,  $l_m/\delta_{cr}$  and mesh size to the geometrical size of the model  $l_m/b$  (Fig. 9), where  $l_m$  denotes mesh size, and  $\delta_{cr}$  denotes critical opening.

The other important parameter is the decohesion length of the cohesive zone,  $l_z$ , defined as

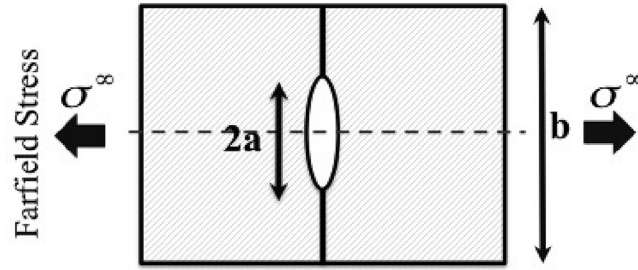


Fig. 9. Collinear crack with periodic boundary conditions.

$$l_z = \frac{9\pi}{32} \left( \frac{E}{1 - \nu^2} \right) \frac{2\gamma_s}{\sigma_{max}^2} \tag{48}$$

where  $2\gamma_s$  denotes the energy release rate and  $\sigma_{max}$  is the maximum traction in the cohesive zone (Falk et al., 2001). From Eq. (48) we find that the length of the cohesive zone is proportional to the inverse square of the maximum traction  $l_z \propto 1/\sigma_{max}^2$ .

We performed several simulations with different ranges of  $\delta_{cr}$ ,  $l_m$ , and  $l_z$  and compared the far-field stress from the simulation with its value calculated from Eq. (45). By comparing the results from the Griffith model, we conclude that:

- The critical opening should be much smaller than the mesh size,  $l_m$  at the crack tip. The adequate range obtained is:  $\frac{1}{100} < \frac{\delta_c}{l_m} < \frac{1}{1000}$
- The mesh length at the crack tip should be significantly smaller than the cohesive zone length, such that  $l_m \ll l_z$ .
- The cohesive zone length should be smaller than the specimen length, such that  $l_z < b$ .

Considering all of these conditions together, we have

$$\frac{\delta_{cr}}{l_m} \ll 1 \ll \frac{l_z}{l_m} < \frac{b}{l_m}. \tag{49}$$

In this work we maintain all parameters within the suggested range by Eq. (49). One of the challenges in modeling the experiment is to maintain intrinsic length scales such as grain size at the same length order as in the experimental sample.

The energy under the traction-separation curve for the cohesive zone is obtained based on the surface energy of copper,  $1 \text{ J/m}^2$ . To keep the value of energy constant, when increasing  $\sigma_{max}$  the critical opening,  $\delta_c$ , must be decreased (cf. Fig. 10). However,  $\delta_c$  physically needs to be the same order as the thickness of the diffusion zone of a grain boundary which we assume to be  $\delta_{gb} = 1 \text{ nm}$  (Wei and Anand, 2004; Péron-Lühns et al., 2013). Considering these inequalities and employing the parameters in Eq. (48), while taking  $\delta_{cr} = 0.8 \text{ nm}$  and  $\sigma_{max} = 500 \text{ MPa}$ , we find a cohesive zone length of  $l_z = 500 \text{ nm}$ . According to Eq. (49), we require that  $l_z \leq b$ , so  $b \geq 500 \text{ nm}$ . Because the value of  $b$  is at least 20 times larger than the experimental value, we consider  $b = 2.5 \mu\text{m}$  for the simulation to satisfy Eq. (49).

The parameters used in this study are set to nondimensionalization groupings shown in Table 3.

### 6.2. Schematic of the model and elements

The 2D model consist of two rectangular grains with periodic boundary conditions (PBC) shown in Fig. 11a. The grains are considered to be the same size and are separated by a grain boundary. Diffusion within the grain boundary occurs inside a “diffusion

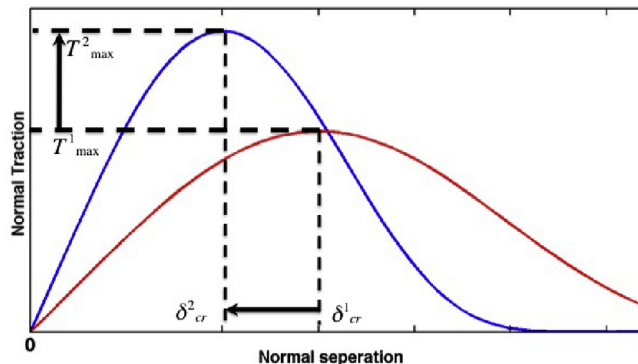
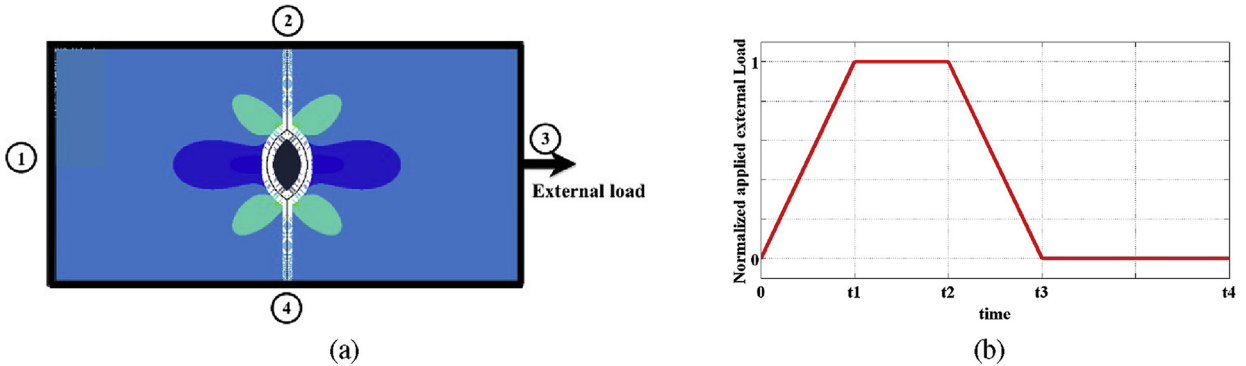


Fig. 10. Change in  $T_{max}$  by changing  $\delta_{cr}$  at constant energy.

**Table 3**  
Nondimensionalization of the material parameters.

|                                   | Parameter Value   | Nondimensionalized Parameter Value  |
|-----------------------------------|---|---|
| Critical opening                  | $\delta_{cr} = 8 \times 10^{-7}$ mm                               | $\bar{\delta}_{cr} = \frac{\delta_{cr}}{\delta_{cr}} = 1$   |
| Initial grain boundary thickness  | $h_{gb} = 1 \times 10^{-6}$ mm                                    | $\bar{h}_{gb} = \frac{h_{gb}}{\delta_{cr}} = 1.25$  |
| GB diffusion coefficient          | $\mathcal{D}_{gb} = 3200 \frac{10^{-3}s}{Kg}$                     | $\bar{\mathcal{D}}_{gb} = \frac{\mathcal{D}_{gb}}{\mathcal{D}_{gb}} = 1$  |
| Surface diffusion coefficient     | $\mathcal{D}_s = 2.8 \times 10^{-6} \frac{10^{-3}s \cdot mm}{Kg}$ | $\bar{\mathcal{D}}_s = \frac{\mathcal{D}_s}{\mathcal{D}_{gb} \delta_{cr}} = \frac{5 \times 2.3 \times 10^{-10}}{0.64 \times 8 \times 10^{-7}} = 0.0225$ |
| Normal Traction (MPa)             | $T_n = 0 - 700$ MPa   | $\bar{T}_n = \frac{T_n}{T_{cr}} = 0 - 1$  |
| Time step                         | $\Delta t$ (s)  | $\bar{\Delta t} = h_l \mathcal{D}_{gb} T_{max} \Delta t = 4.48 \times 10^{-4} \Delta t$   |
| Atomic diffusion flux for GB      | $j_{gb} (\text{mm}^{-1} \text{s}^{-1})$                           | $\bar{j}_{gb} = \frac{j_{gb}}{T_{max} \mathcal{D}_{gb}} \bar{h}_{lgb} = 2.66 \times 10^{-3} j_{gb}$   |
| Atomic diffusion flux for surface | $j_s (\text{mm}^{-1} \text{s}^{-1})$                              | $\bar{j}_s = \frac{j_s}{T_{max} \mathcal{D}_{gb}} \bar{h}_{lgb} = 2.66 \times 10^{-3} j_s$  |
| Length scale                      | $ds = 2.97 \times 10^{-6} - 8.96 \times 10^{-5}$ mm               | $\bar{ds} = \frac{ds}{h_{lgb}} = 2.97 - 89.6$   |
| Atomic volume                     | $\Omega = 1.18 \times 10^{-20}$ mm <sup>3</sup>                   | $\bar{\Omega} = \frac{\Omega}{h_{lgb}^3} = 0.023$   |
| Curvature of void                 | $\kappa \sim 1450 \text{mm}^{-1}$                                 | $\bar{\kappa} = \kappa \times \delta_{cr} = \kappa \times 8 \times 10^{-7}$   |
| Surface energy                    | $\gamma_s$ (N/m)  | $\bar{\gamma}_s = \frac{\gamma_s}{\delta_{cr} T_{max}} = 1.78$  |
| Chemical potential of GB          | $\mu_{gb} (10^3 \text{Kgmm}^2 \text{s}^{-2})$                     | $\bar{\mu}_{gb} = \frac{\mu_{gb}}{T_{max} h_l^3} = \mu_{gb} \times \frac{10^{18}}{700}$   |
| Chemical potential of surface     | $\mu_s (10^3 \text{Kgmm}^2 \text{s}^{-2})$                        | $\bar{\mu}_s = \frac{\mu_s}{T_{max} h_l^3} = \mu_s \times \frac{10^{18}}{700}$  |



**Fig. 11.** a) Schematic of the model used in simulation; b) External load applied to the model system.

zone.” A pre-existing void is assumed to be in the middle of the grain boundary. The deformation mechanisms are assumed to be isotropic linear elastic-plastic deformation within the grains, diffusion within the grain boundary, and the possibility of decohesion along the grain boundary. Periodic boundary conditions are applied on the edges of the grain (cf. Fig. 11a).

The 2D model is meshed inside the grains and along the grain boundary. The mesh size is refined in the vicinity of the void tip for both grains and grain boundaries (Fig. 12). According to length scale arguments discussed in Section 6.1, the value for the smallest mesh length is defined to be at about one order of magnitude larger than the value for the critical-opening of grain boundary,  $\delta_{cr}$ . The value is refined to about 3 nm for the mesh at the void tip in the gain boundary. We increased the mesh size with about an order and did not find significant change in the results, which shows that the results are not mesh sensitive. The critical opening is determined by defining the potential function for the cohesive zone. The elements used within the grains are 8-node biquadratic plane strain elements (CPE8R) selected from the ABAQUS element library. The cohesive zone elements of the grain boundary are defined by six-nodes in one-dimensional elements. The shape function is prescribed by a quadratic polynomial equation over each element. The diffusion zone is meshed by defining two-node linear elements.

The constitutive equations used to model the cohesive zone and diffusion inside the grain boundary are implemented in commercial finite element analysis (FEA) software ABAQUS<sup>®</sup> using a user defined subroutine (UEL) based on Eq. (38) and Eq. (42).

An external force is applied on the right side of the model (Fig. 13) which induces a uniform displacement imposed in the  $x_1$ -direction for all nodes at the edge. Fig. 11b shows the applied load versus time in the experiment. The load gradually increases from zero to its maximum over a period of time  $t_1$ . The value of  $t_1$  is adjusted to match the experimentally applied strain-rate. The value for the maximum external load also matches the experiments. The dwell time is defined from  $t_1$  to  $t_2$  when the external load is

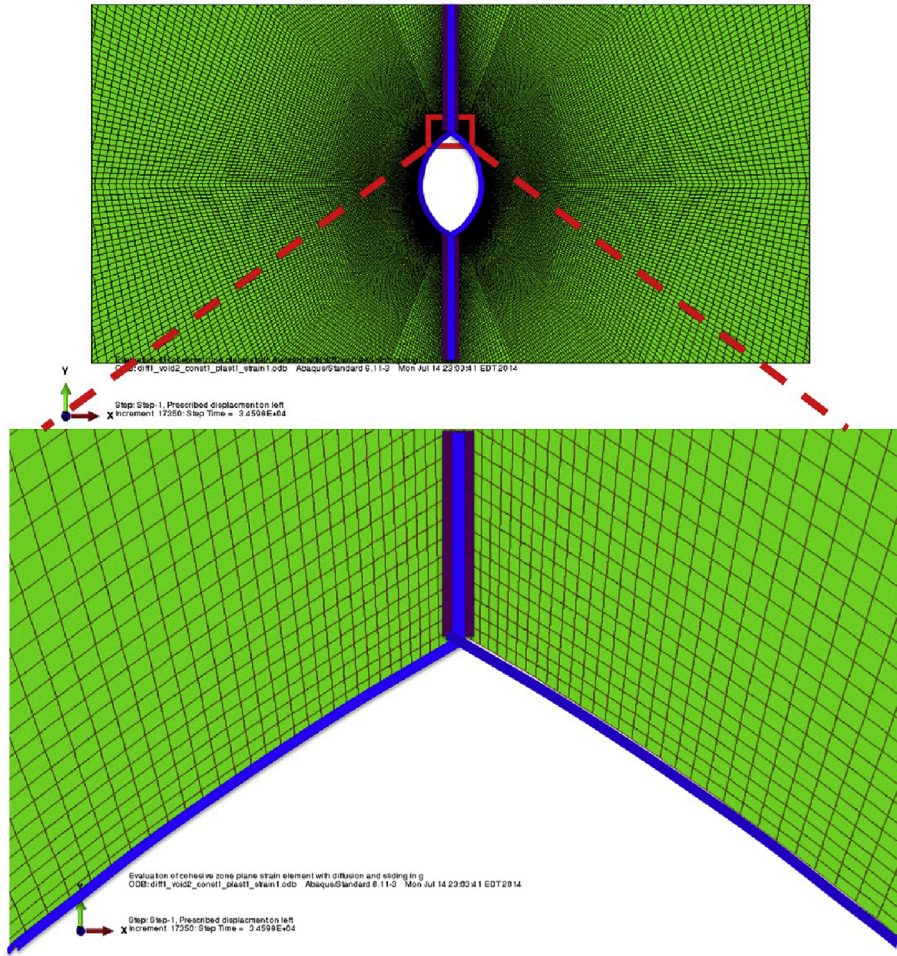


Fig. 12. Schematic of the mesh of the model. Purple lines represent the cohesive zone region and blue lines show diffusion zone region. (For interpretation of the references to colour in this figure legend, the reader is referred to the Web version of this article.)

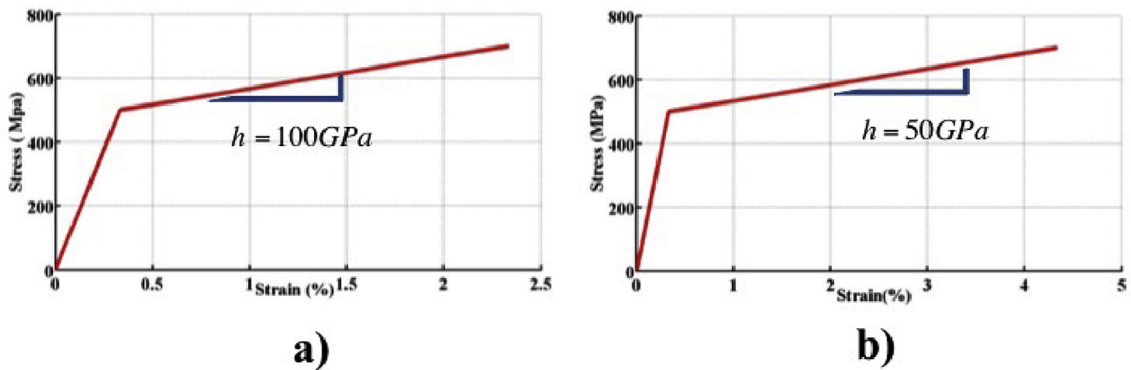


Fig. 13. Elastic-plastic behavior for nanocrystalline copper applied in the simulation: a) 100 GPa hardening rate, b) 50 GPa hardening rate.

kept constant. The external load is then gradually released from its maximum to zero from time  $t_2$  to  $t_3$ . From  $t_3$  to  $t_4$  there are no external forces on the sample.

Plastic strain recovery begins after the unloading part of the load cycle, but most of the strain recovery occurs while no external loads are applied to the virtual sample. Plastic strain recovery rate as a function of time is calculated by comparing the instantaneous thin film length at any time after  $t > t_3$  to the length of the film immediately after unloading at  $t = t_3$ .

**Table 4**  
PPR cohesive zone parameters employed in this study.

|   |                                    |                   |
|---|------------------------------------|-------------------|
| Normal critical displacement              | $\delta_{nc}$                      | 0.85 nm           |
| Tangential critical displacement          | $\delta_{tc}$                      | 0.85 nm           |
| Initial Normal slope indicator            | $\lambda_n$                        | $\frac{1}{3}$     |
| Initial Tangential slope indicator        | $\lambda_t$                        | $\frac{1}{3}$     |
| Initial grain boundary thickness          | $h_0$                              | 1 nm              |
| Mode I fracture energy                    | $\phi_n$                           | 1J/m <sup>2</sup> |
| Mode II fracture energy                   | $\phi_t$                           | 1J/m <sup>2</sup> |
| Shape parameter in the PPR model          | $\alpha$                           | 5                 |
| Shape parameter in the PPR model          | $\beta$                            | 5                 |
| Normal characteristic length scale        | $\delta_n = \lambda_n \delta_{nc}$ | 2.25 nm           |
| Tangential characteristic length scale    | $\delta_t = \lambda_t \delta_{tc}$ | 2.25 nm           |
| Max Normal Stress Parameter               | $\sigma_{max}$                     | 835 MPa           |
| Max Shear Stress Parameter                | $\tau_{max}$                       | 835 MPa           |
| Non-dimensional exponent in the PPR model | $m$                                | 4.7816            |
| Non-dimensional exponent in the PPR model | $n$                                | 4.7816            |

### 6.3. Element properties

#### 6.3.1. Material properties of the grain

The material properties inside the grain are defined to be elastic-plastic with Young Modulus,  $E$ , of bulk copper of 135 GPa (Wei et al., 2007) and the Poisson ratio is taken to be  $\nu = 0.35$  (ASM International, 1990). The conventional plastic deformation mechanisms inside the grains for nanocrystalline materials are constrained compared to in coarse grain materials, resulting in higher yield stress in nanocrystalline materials. In our model, yield stress is assumed to be 550 MPa (Yilmaz and Kysar, 2013) which is higher than the yield stress for microcrystalline copper (about 300 MPa (Xiang et al., 2006)). Plastic deformation is limited only to the regions close to the void tip where there is local stress concentration. Fig. 13 shows two sets of elastic-plastic behavior employed in this study.

#### 6.3.2. Cohesive zone in grain boundary

We define eight characteristic parameters, specifically  $\Gamma_n$ ,  $\Gamma_t$ ,  $m$ ,  $n$ ,  $\delta_n$ ,  $\delta_t$ ,  $\alpha$ , and  $\beta$  to prescribe the parameters for the PPR potential function for the cohesive zone. All other parameters in the cohesive zone can be related to these eight parameters. The list of parameters and their values used in this work are shown in Table 4. The critical opening,  $\delta_c$ , is defined to be in the same order as grain boundary thickness of 1 nm (Wei and Anand, 2004; Péron-Lührs et al., 2013). Additionally, the maximum strength,  $\sigma_{max}$ , is prescribed to be slightly higher than the yield stress of the copper to ensure plastic deformation can be induced in the grains.

#### 6.3.3. Diffusion in grain boundary

The parameters for the diffusion zone (DZ) within the grain boundary are listed in Table 5. The value for the grain boundary diffusivity of copper is  $\delta_{gb} D_{gb} = 8.36 \times 10^{-30} \text{ m}^3/\text{s}$  where  $\delta_{gb} = 1 \text{ nm}$  is the thickness of the diffusion zone in the grain boundary as obtained from our creep test (Ghazi and Kysar, 2016). This value is in good agreement with the grain boundary diffusion for nanocrystalline materials (Wei et al., 2008b) and is about four orders of magnitude higher than the grain boundary diffusion for microcrystalline copper (Thouless, 1993). The temperature is assumed to be ambient.

### 6.4. Grain boundary behavior at void tip

Simulation results for normal traction, diffusion flux, incremental change in grain boundary thickness, and total change in grain boundary thickness are shown at different time steps (cf. Fig. 14). These parameters are explored in the grain boundary region close to the void tip. This region includes only about 2% of the grain boundary length denoted as  $L$ . The diffusion flux,  $j$ , on grain boundary is defined to be positive in the direction shown in Fig. 14. The direction of flux at the void tip depends on the difference between surface and grain boundary chemical potentials. The change in chemical potential of the surface depends upon curvature (Eq. (11)).

**Table 5**  
Values for parameters related to inelastic deformation mechanisms.

|   | case 1            | case 2            | case 3            | case 4            | case 5            | case 6            |
|---|-------------------|-------------------|-------------------|-------------------|-------------------|-------------------|
| Diffusion Coefficient (mm <sup>2</sup> /s)                              | 10 <sup>-14</sup> | 10 <sup>-16</sup> | 10 <sup>-14</sup> | 10 <sup>-14</sup> | 10 <sup>-14</sup> | 10 <sup>-14</sup> |
| Diffusion constant at void tip (s/(10 <sup>3</sup> Kgmm <sup>3</sup> )) | 1                 | 1                 | 5                 | 1                 | 1                 | 1                 |
| Plasticity hardness (GPa)   | $h = 100$ .       | $h = 100$         | $h = 100$         | $h = 50$          | $h = 100$         | $h = 100$         |
| Void value fraction   | 0.27%             | 0.27%             | 0.27%             | 0.27%             | 2.4%              | 0.27%             |
| Strain rate for loading (1/s)   | 10 <sup>-5</sup>  | 10 <sup>-4</sup>  |

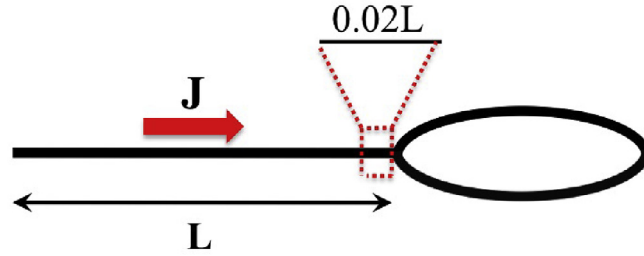


Fig. 14. Grain boundary region close to the void tip ( $L$  is length of the grain).

The rate of change in curvature is negligible in this work and therefore the surface chemical potential is considered constant, so the flux at the void tip is mainly governed by change in chemical potential of the grain boundary and directly affected by normal traction on the grain boundary close to the void tip.

### 7. Simulation of load cycle and recovery

#### 7.1. Loading phase

The simulation results on a portion of the grain boundary very close to the void tip, where the void tip is at position  $L$  along the grain boundary are illustrated in Fig. 15. Results are shown at three simulation times: the beginning of loading ( $t = 0$ ), the middle of loading ( $t = t_1/2$ ), and the end of loading ( $t = t_1$ ). In Fig. 15a, the normal traction in grain boundary at  $t = 0$  is zero everywhere on the grain boundary. At  $t = t_1/2$  there is a significant stress concentration near the void tip inducing a positive gradient of traction along the boundary. At  $t = t_1$  the peak normal traction is equal to  $\sigma_{max}$  at about  $0.996L$  and normal traction decreases as the void tip is approached. This finding indicates that the deformation state in the grain boundary between the point of peak normal traction and the void tip is such that the cohesive zone separation exceeds the critical cohesive zone separation,  $\delta_{cr}$ , and results in normal traction decrease (cf. Fig. 10).

Fig. 15b shows the direction and magnitude of diffusion flux for the nodes close to the void tip. At  $t = 0$  there is no diffusive flux since the traction gradient is zero. At  $t = t_1/2$  the flux is positive which indicates a net mass flux along the grain boundary toward the

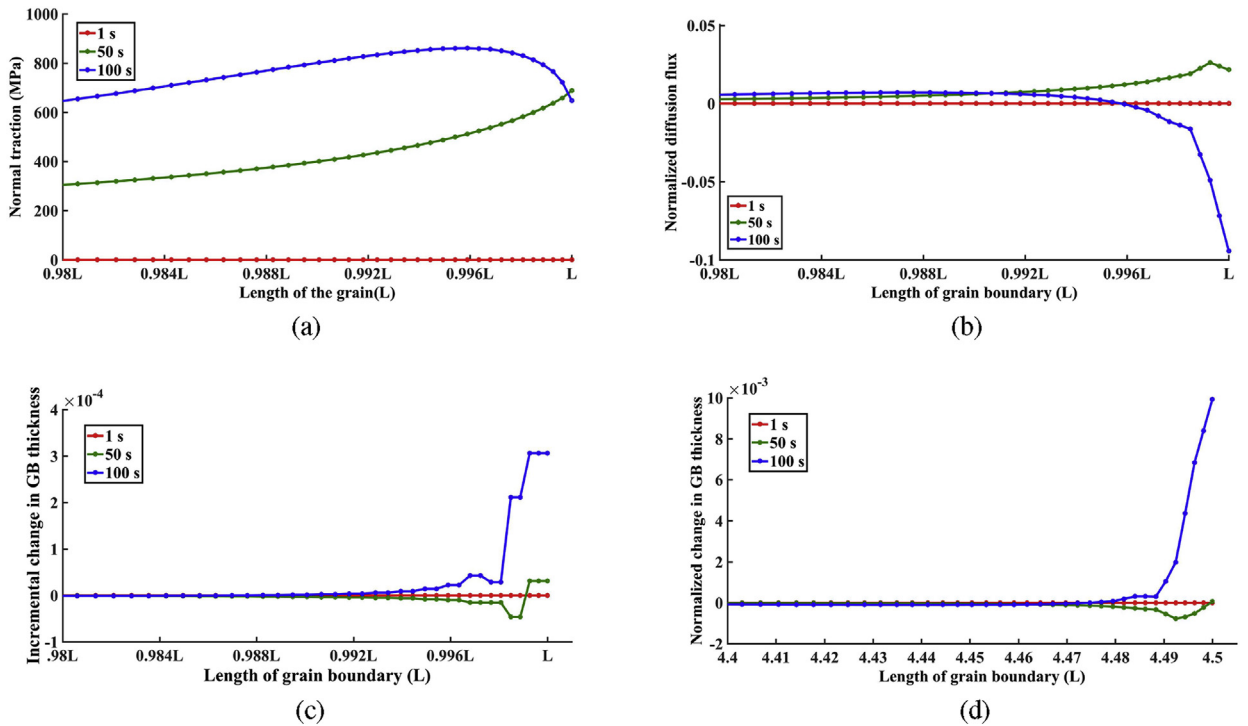


Fig. 15. Simulation results close to the void tip as a result of external loading from  $t = 0$  to  $t = t_1(100s)$ : a) Normal traction over grain boundary close to the void tip; b) Diffusion flux along grain boundary; c) Incremental change in grain boundary thickness due to diffusion; d) Total change in grain boundary thickness.

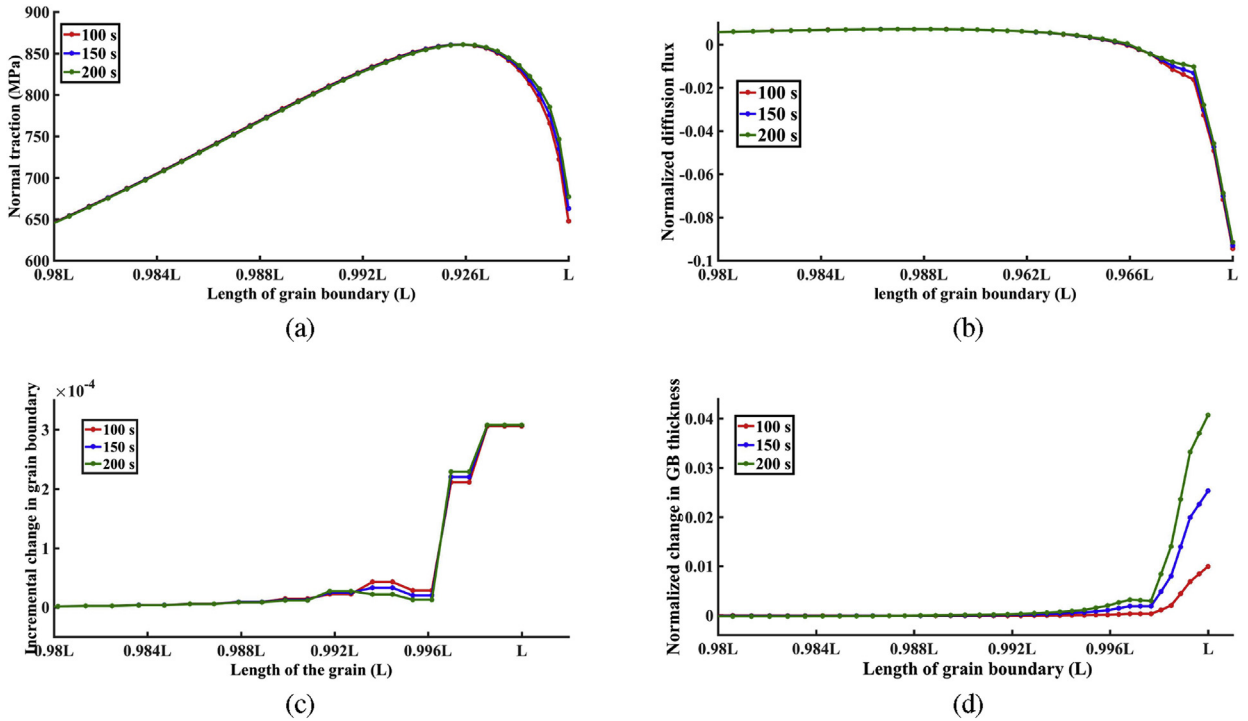


Fig. 16. Dwell period of constant external force from  $t_1(100\text{ s})$  to  $t_2(200\text{ s})$ : a) Normal Traction over grain boundary close to the void tip; b) Diffusion flux over grain boundary close to the void tip; c) Incremental change in grain boundary thickness due to diffusion over grain boundary close to the void tip; and, d) Total change in grain boundary thickness due to diffusion over grain boundary close to the void tip.

void tip. At  $t = t_1$  the mass flux is negative between  $0.996L$  and the void tip and otherwise positive indicating a net mass flux away from the void tip between  $0.996L$  and the void tip. Fig. 15b exhibits sharp changes in slope at  $t = t_1/2$  and  $t = t_1$  very near the void tip due to mass flux from the void surface to the grain boundary which contributes a negative flux in that region (Fig. 20). This flux is caused by the difference between the chemical potential of the void surface and grain boundary described in Eq. (17). We note that, at the beginning of the loading step, to avoid singularity caused by the flux jump between the grain boundary and the surface at the void tip, we prescribed  $C$  to be very small and gradually increased it to its final value  $C$ . The results were not sensitive to how we activated and subsequently increased the void tip flux condition.

Fig. 15c, and d shows the change in thickness in the current time step and the overall thickness of the diffusion zone, respectively, along the grain boundary. At  $t = t_1$  in Fig. 15d the thickness of the diffusion zone increases significantly due to a combination of grain boundary flux toward the tip as well as flux from the void surface to the near-tip grain boundary region. The accumulation of mass in this region plays an important mechanistic role in the phenomenon of plastic strain recovery.

### 7.2. Load dwell phase

Fig. 16a, b, and c show behavior during the dwell time from  $t_1 \leq t \leq t_2$  when the external force is kept constant. We see that the grain boundary traction and the flux change very little during the load dwell. However since the gradient of diffusion remains negative, the accumulation of mass in the near void tip region continues unabated which leads to an increase in the diffusion zone thickness (Fig. 16-d) and ultimately increases the diffusion zone thickness by up to 3%.

### 7.3. Unloading phase

During the unloading phase the external load decreases linearly over time to a zero external load from  $t_2 = 200\text{ s}$  to  $t_3 = 300\text{ s}$ . Fig. 17a shows the normal traction on the grain boundary at three time steps during unloading. At the end of the unloading phase, the material is not under any external stress, but the simulation results show that a compressive residual traction has developed along the grain boundary at the void tip. The additional mass that diffused into the near void tip region during the loading and dwell phases causes this increase in diffusion zone width. Upon unloading, the presence of the additional mass in the near tip region induces a compressive traction on the grain boundary. The direction of net diffusion flux in the near void tip region changes as a result of the compressive traction (Fig. 17b). Because of this directional change, the diffusion zone thickness decreases slightly during the unloading phase (cf. Fig. 17).

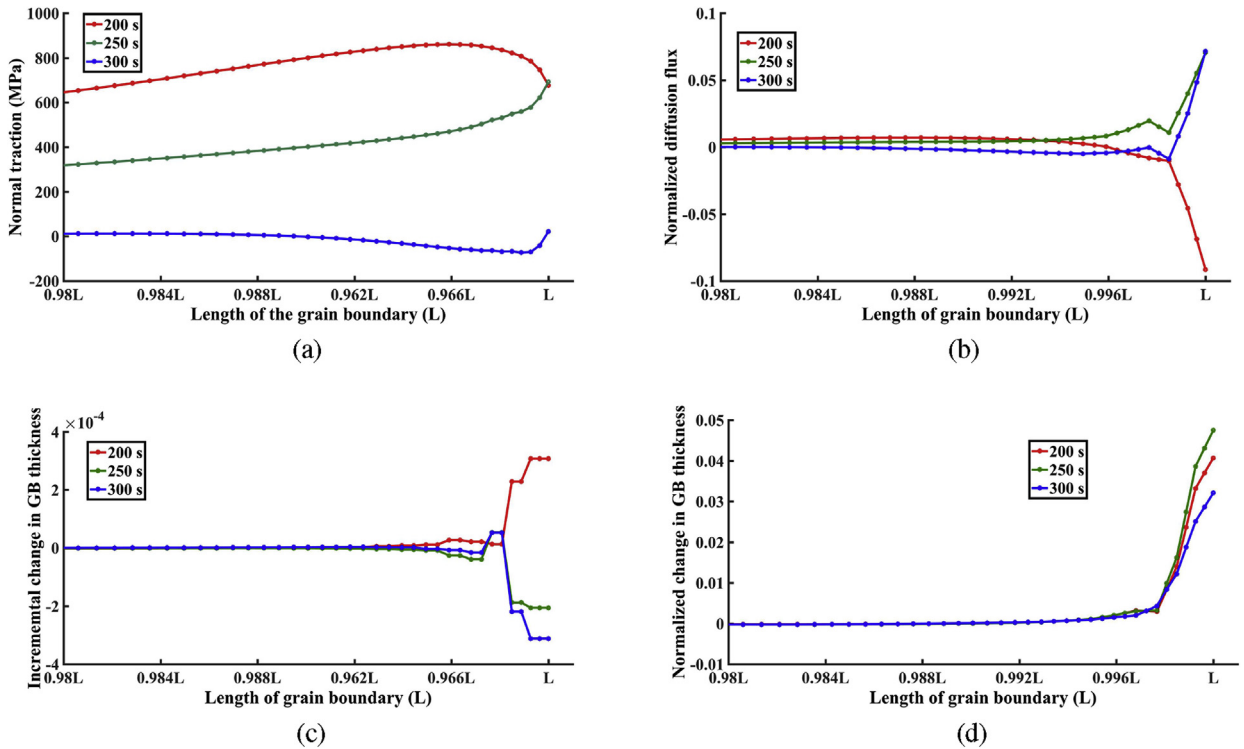


Fig. 17. Unloading external force from  $t_2$  (200 s) to  $t_3$  (300 s): a) Normal Traction over grain boundary close to the void tip; b) Diffusion flux over grain boundary close to the void tip; c) Incremental change in grain boundary thickness due to diffusion over grain boundary close to the void tip; and, d) Total change in grain boundary thickness due to diffusion over grain boundary close to the void tip.

#### 7.4. Recovery phase

Diffusion flux along the grain boundary continues after the external load is removed due to the compressive traction on the grain boundary near the void tip as well as the jump in chemical potential from the grain boundary to the void surface. Fig. 18 and Fig. 19 present the normal traction, the diffusion flux, and the change in diffusion zone thickness from  $t_3$  to  $t_4$  for two different void ratios of 0.27% and 2.4%, respectively. For both ratios the trend is the same: atoms accumulated near the void tip of the grain boundary during the loading, dwelling, and unloading steps diffuse back to the void surface and also away from the near void tip region of the grain boundary (Fig. 20).

At  $t = t_3 = 300$  s the positive sign of diffusion flux at the void tip in Fig. 18-b and 19-b indicates that the direction of flux is from the grain boundary to the void surface. Further to the left in the same figures the sign for flux is negative. Both fluxes reduce the thickness of the diffusion zone near the void tip as can be seen in Fig. 18-d and Fig. 19-d. At a critical time of  $t \approx 400$  s, the diffusion zone has recovered its initial thickness after which very little diffusion flux is driven away from the near void tip toward the left. Subsequent flux away from the near void tip region is driven by the jump in chemical potential from the grain boundary region to the void surface in order to fill up the void. However since the change in the void size compared to its initial dimension is negligible, the void ratio is considered to be constant during recovery. This flux is sufficient to decrease the thickness of the diffusion zone until there is a tensile stress in the near void tip region.

The experiments demonstrate both transient as well as a steady-state plastic strain recovery rates. Our computational results suggest that the faster transient plastic strain recovery rate is due to the combination of flux away from the near void tip region along the grain boundary as well as toward the void surface. The transition from transient plastic strain recovery rate to the slower steady state plastic strain recovery rate occurs when the diffusion zone thickness has recovered its initial thickness (at  $t \approx 400$  s in the simulations). Afterwards the only flux away from the near void tip region is to the void surface which explains why the steady-state plastic strain recovery rate is slower than the transient rate. During the transient process, the diffusion is driven by a combination of compressive normal stress and the jump in chemical potential from the grain boundary to the void surface resulting in “fast” strain recovery rates. As time progresses, the compressive stress decreases which leads to a reduction in plastic strain recovery.

### 8. Influence of different parameters

We performed a series of simulations to explore the effect of the following parameters on plastic strain recovery rate:

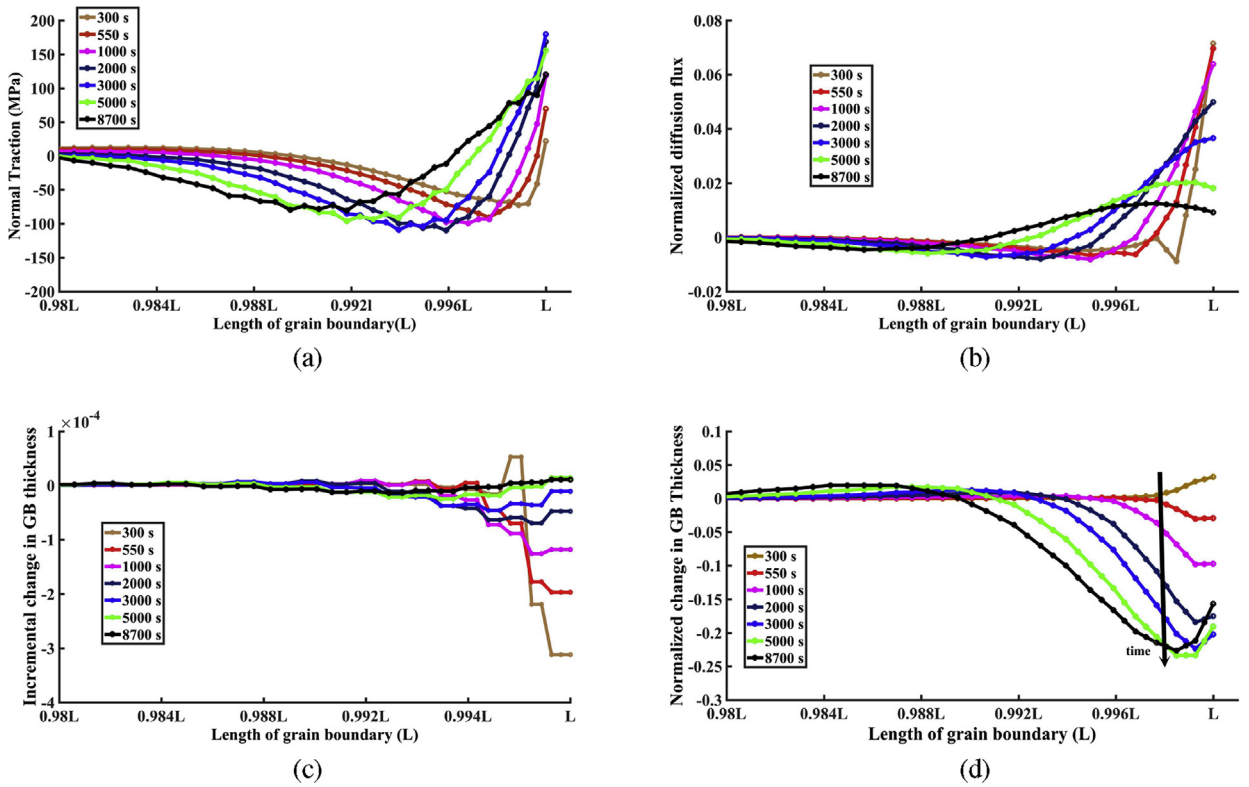


Fig. 18. Results of simulation with void ratio 0.27% in the plastic strain recovery phase from  $t_3(300\text{ s})$  to  $t_4$ : a) Normal Traction over grain boundary close to the void tip; b) Diffusion flux over grain boundary close to the void tip; c) Incremental change in grain boundary thickness due to diffusion over grain boundary close to the void tip; d) Total change in grain boundary thickness due to diffusion over grain boundary close to the void tip.

- Diffusion coefficient of the grain boundary:  $D_{gb}$
- Plasticity hardening rate inside the grains (cf. Fig. 13)
- Volume fraction of pre-existing void
- Strain rate during loading
- Diffusion coefficient between the grain boundary and surface at the void tip  $C$ .

The values for these parameters are shown in Table 5.

Simulations are performed for each parameter in Table 5 for two values, the “base value” (case 1) which represents the magnitude of the parameter close to the experimental value, and new values to explore the effect of change of the parameter (cases 2 through case 6). Simulations results (Fig. 21) show that plastic strain recovery occurs at two different characteristic rate – an initial faster transient rate followed by a slower steady state rate – similar to what was observed in (Ghazi and Kysar, 2016). Plastic strain recovery rate as a function of time is calculated by comparing the instantaneous thin film length at any time after  $t > t_3$  to the length of the film immediately after unloading  $t = t_3$  which results in the negative strain in Fig. 21.

Plastic strain rate recovery results and duration are presented in Table 6.

- By comparing the results from Case 1 and Case 2 we conclude that plastic strain recovery is more significant with a higher diffusion coefficient. It should be noted again that the diffusion coefficient in nanocrystalline metals is four orders of magnitudes higher than the diffusion coefficient in coarse grained metals (Rajagopalan et al., 2007; WeiKysar, 2011).
- We observe no effect on the overall recovery rates for different diffusion constants at the void tip in Cases 1 and 3.
- The calculated plastic strain recovery rate indicates that increasing the plastic hardening between Cases 1 and 4 causes the recovery to be slightly faster at the beginning with a subsequent sharp slow down.
- The simulations show that increasing the void fraction causes an increase in the recovery rate (Case 1 compared to Case 5). The recovery rate and duration for Case 5 is in agreement with previous experimental studies and suggests that the ratio for porosity and void in our sample is close to the value used in our simulation.
- Our results show that decreasing strain rate during loading does not affect the recovery rate (Case 1 compared to Case 6).

The strain recovery behavior for all cases is shown in Fig. 22.

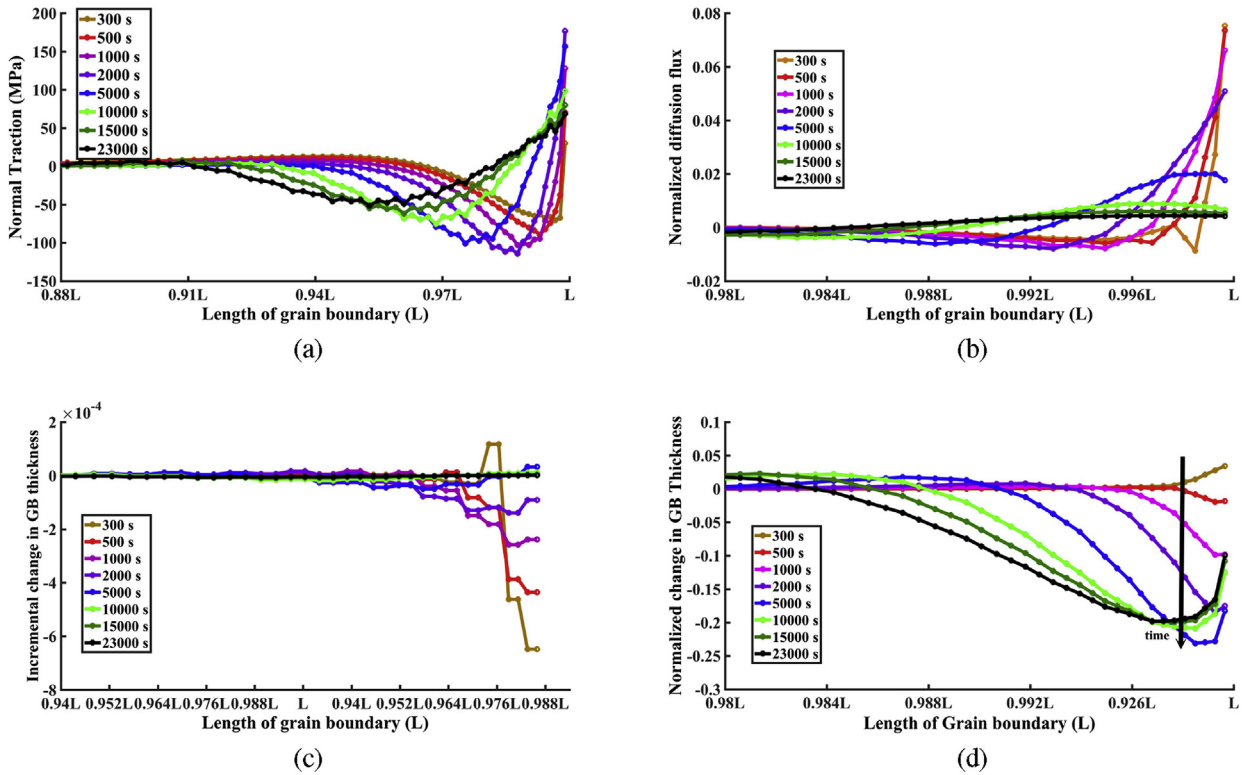


Fig. 19. Results of simulation with void ratio 2.4% in the plastic strain recovery phase from  $t_3$  (300 s) to  $t_4$ : a) Normal Traction over grain boundary close to the void tip; b) Diffusion flux over grain boundary close to the void tip; c) Incremental change in grain boundary thickness due to diffusion over grain boundary close to the void tip; and, d) Total change in grain boundary thickness due to diffusion over grain boundary close to the void tip.

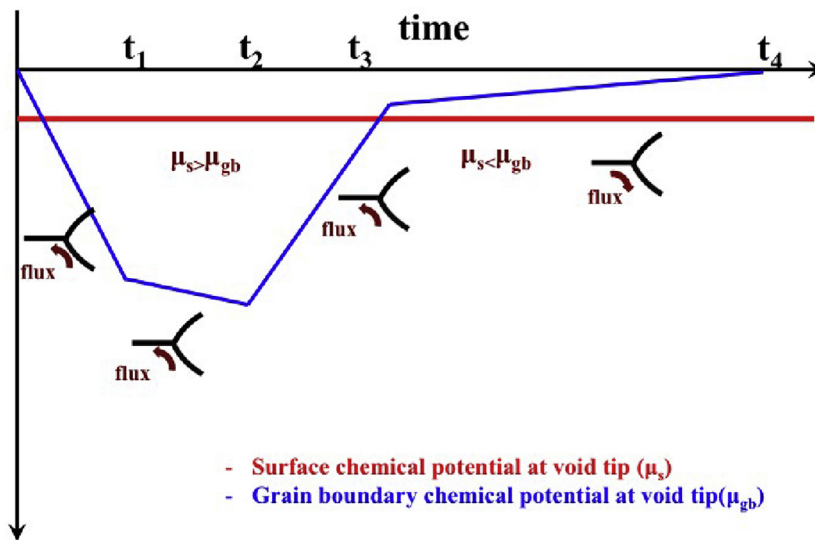


Fig. 20. Direction of atomic flux between surface and grain boundary at void tip over time during loading ( $t_0-t_1$ ) Dwell time ( $t_1-t_2$ ) unloading ( $t_2-t_3$ ) and recovery ( $t_3-t_4$ ).

9. Conclusions

In this work we develop a mechanistic model for plastic strain recovery in nanocrystalline copper thin films and compare the results to experimental observations in (Ghazi and Kysar, 2016). The dominant inelastic deformation mechanism in the model is grain boundary diffusion, driven by chemical potential gradients resulting from residual stresses and the presence of pre-existing voids in

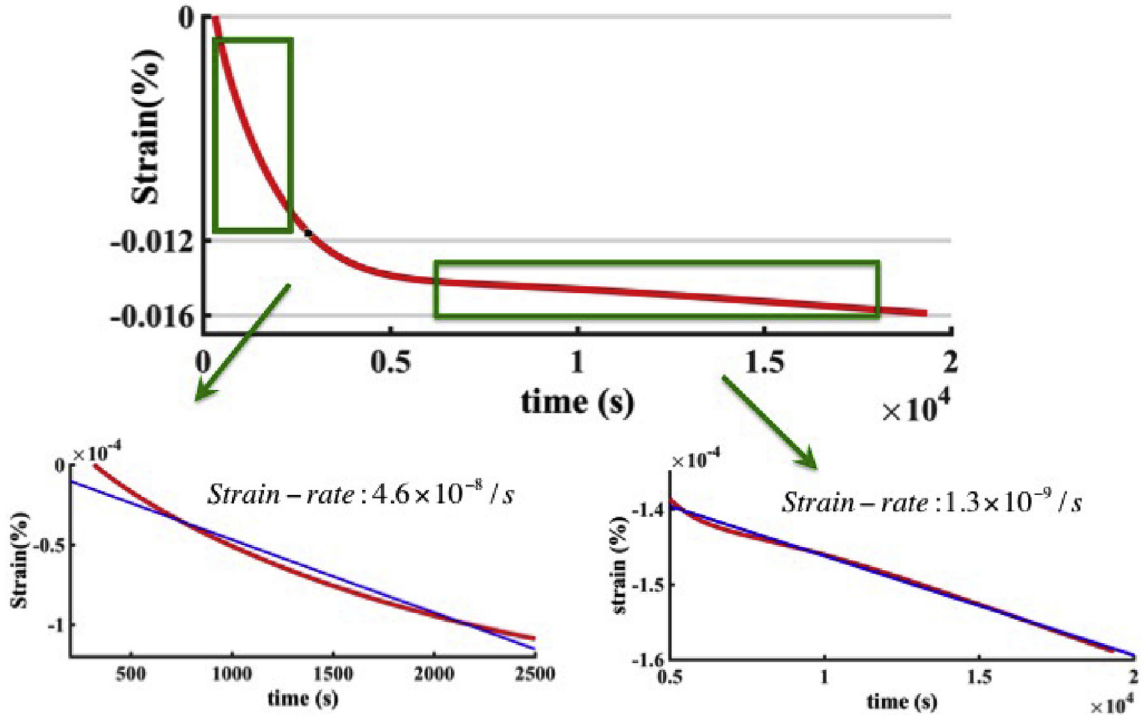


Fig. 21. Plastic strain recovery in the simulation with 2.4% void volume ration (N.B. zero time here corresponds to  $t_3$ ).

**Table 6**  
Sets of parameters employed in plastic strain recovery simulations.

|        |                    | Residual strain (%)  | first strain recovery rate (1/s) | first recovery time (s) | second strain recovery rate (1/s) |
|--------|--------------------|----------------------|----------------------------------|-------------------------|-----------------------------------|
| Case 1 | 1-Base             | $10^{-5}$            | $7 \times 10^{-9}$               | 3000                    | $2 \times 10^{-10}$               |
| Case 2 | 2-Diff_coefficient | $9 \times 10^{-6}$   | $9.5 \times 10^{-11}$            | -                       | $9.5 \times 10^{-11}$             |
| Case 3 | 3-C-void tip 2     | $1.3 \times 10^{-5}$ | $7 \times 10^{-9}$               | 3000                    | $2.9 \times 10^{-10}$             |
| Case 4 | 4-Hardness 2       | $1.3 \times 10^{-5}$ | $1.1 \times 10^{-8}$             | 2500                    | $1.9 \times 10^{-11}$             |
| Case 5 | 5-Void fraction 2  | $11 \times 10^{-5}$  | $6.8 \times 10^{-8}$             | 4000                    | $2.5 \times 10^{-9}$              |
| Case 6 | 6-Loading rate 2   | $1.1 \times 10^{-5}$ | $4.8 \times 10^{-9}$             | 4000                    | $2 \times 10^{-10}$               |

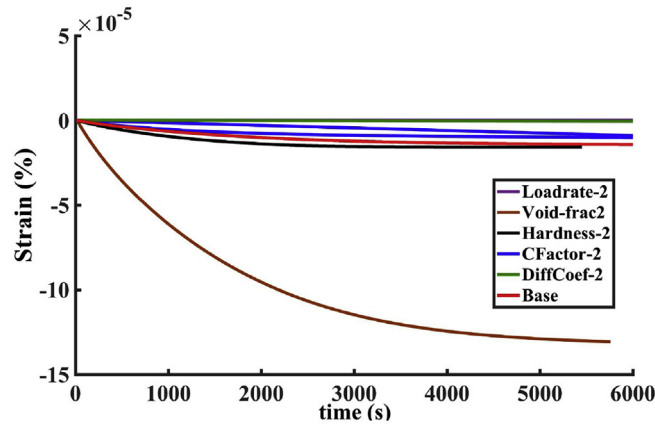


Fig. 22. Plastic strain recovery rate for all parameters.

the film. We incorporate a diffusion zone and cohesive zone associated with the grain boundary and a diffusion zone associated with the void surface. The diffusion zone admits deformation by accounting for the driving forces of atomic diffusion over the grain boundary and void surface to determine the direction and magnitude of atomic flux within the grain boundary. A cohesive zone is

also associated with the grain boundary to admit deformation via a traction-separation constitutive behavior of the grain boundary defined by a potential function.

The non-linear constitutive equations for deformation behavior inside the grain boundary and void surface are implemented through a user element (UEL) subroutine in the commercial finite element code ABAQUS/Standard. We use the Griffith model to identify acceptable ranges of parameters for the diffusion zone and the cohesive zone in the context of mesh size and decohesion length of the cohesive zone. We perform a series of simulations to explore the effects on plane strain recovery rate of parameters such as grain boundary diffusion coefficient, void to model length ratio, plastic hardening rate, and gradient of flux at void tip. The results for all simulations display two characteristic plastic strain recovery rates: an initial faster transient rate followed by a slower steady state rate. This findings is consistent with previous experimental results (Ghazi and Kysar, 2016; Wei et al., 2007).

Our model suggests that external tensile loading of the system activates diffusion mechanisms that lead to a build-up of surplus material in the region very near the tips of voids. The surplus material is transported via a net diffusion flux on the grain boundary toward the void tip as well as a net diffusion flux from the void surface to the region very near the void tip. Upon removal of the external loads, the surplus material generates a compressive residual stress normal to the grain boundary near the void tip. The normal stress induces diffusion flux away from the void tip. At first two diffusion fluxes are active: the compressive residual stress drives a net diffusion flux on the grain boundary away from the void tip, and the jump in chemical potential between the grain boundary and the void surface drives a net flux from the grain boundary to the void surface. The specimen shortens as a consequence of these diffusion mechanisms which manifests itself experimentally as plastic strain recovery. Activation of the two diffusion mechanisms leads to a gradual decrease of compressive residual stress on the grain boundary near the void tip. Once the compressive stress—and the related stress gradients—decrease sufficiently, the diffusion flux from the grain boundary to the void surface is the dominant deformation mechanism, and the resulting smaller magnitude of the overall diffusion flux leads to the slower characteristic rate of plastic strain recovery.

### Acknowledgements

NG and JWK gratefully acknowledge support from the National Science Foundation (DMR-1310503). CFN is financially supported by The Danish Council for Independent Research project “New Advances in Steady-State Engineering Techniques”, grant DFF-4184-00122.

### Appendix 1

The virtual work of this process is

$$\int_s (T^n \delta u^n + T^t \delta u^t) ds \tag{50}$$

which represents the cohesive surface energy. This term considers the effect of normal ( $T^n$ ) and tangential ( $T^t$ ) traction on the corresponding cohesive surface.

$T^n$  and  $T^t$  can be rearranged by defining  $a_n$  and  $a_t$  as

$$T^n = T^n(\Delta n, \Delta t) = a^n(\Delta n, \Delta t) \times \Delta n \tag{51}$$

$$T^t = T^t(\Delta n, \Delta t) = a^t(\Delta n, \Delta t) \times \Delta t \tag{52}$$

where  $\Delta n = (u^n - (h - h_0))$ ,  $\Delta t = (u^t - u^s)$ ,  $h$  is the current grain boundary thickness,  $h_0$  is the initial grain boundary thickness, and  $u^s$  is the relative displacement across the grain boundary. By substituting  $T^n$  and  $T^t$  into the Eq. (50), the contribution of the cohesive zone element to the principle virtual work is obtained as

$$\int (a^n u^n \delta u^n + a^t u^t \delta u^t) ds - \int (a^n (h - h_0) \delta u^n + a^t u^s \delta u^t) ds. \tag{53}$$

Using the discretized form of  $u^n$  and  $u^t$  from Eq. (53) and Eq. (22) we can rewrite Eq. (53) as

$$\int (a^n (n_i Q_{iL}) U_L (n_j Q_{jK}) \delta U_K + a^t (t_i Q_{iL}) U_L (t_j Q_{jK}) \delta U_K) ds - \int (a^n (h - h_0) (n_j Q_{jK}) \delta U_K + a^t (t_j Q_{jK}) \delta U_K) ds \tag{54}$$

where summation over the lower indices  $K$  and  $L$  is implied. Thus Eq. (54) has the final form

$$K_{KL} U_L - f_k \tag{55}$$

where the matrix  $K$  and the vector  $f$  are

$$K_{KL} = \int [a^n (n_j Q_{jK})(n_i Q_{iL}) + a^t (t_j Q_{jK})(t_i Q_{iL})] ds \tag{56}$$

$$f_k = \int [a^n (n_j Q_{jK})(h - h_0) + a^t (t_j Q_{jK})(u^s)] ds. \tag{57}$$

By substituting Eq. (5) and Eq. (6) in Eq. (51) and Eq. (52),  $a_n$  and  $a_t$  are found as

$$a_n(\Delta n, \Delta t) = -\frac{\Gamma_n}{\delta n^2} \left(1 - \frac{\Delta n}{\delta n}\right)^{\alpha-1} \left(\frac{m}{\alpha} + \frac{\Delta n}{\delta n}\right)^{m-1} \times (m + \alpha) \times \left[ \Gamma_t \left(1 - \frac{|\Delta t|}{\delta t}\right)^\beta \left(\frac{n}{\beta} + \frac{|\Delta t|}{\delta t}\right)^n + \langle \phi_t - \phi_n \rangle \right] \tag{58}$$

$$a_t(\Delta n, \Delta t) = -\frac{\Gamma_t}{\delta t^2} \left(1 - \frac{|\Delta t|}{\delta t}\right)^{\beta-1} \left(\frac{n}{\beta} + \frac{|\Delta t|}{\delta t}\right)^{n-1} \times (n + \beta) \times \left[ \Gamma_n \left(1 - \frac{\Delta n}{\delta n}\right)^\alpha \left(\frac{m}{\alpha} + \frac{\Delta n}{\delta n}\right)^m + \langle \phi_n - \phi_t \rangle \right]. \tag{59}$$

The tangential stiffness matrix ( $T$ ) is obtained by using the Newton-Raphson definition as

$$T_{kl} = K_{kl} + \sum \frac{\partial K_{km}}{\partial U_l} U_m - \frac{\partial f_k}{\partial U_l} \tag{60}$$

where  $K$  and  $f$  are found from Eqs. (30) and (31). The derivative of matrix  $K$  to the field variable at nodes "U" is

$$\frac{\partial K_{km}}{\partial U_l} = \int \left[ \frac{\partial a^n}{\partial U_l} (n_j Q_{jk})(n_l Q_{lm}) + \frac{\partial a^t}{\partial U_l} (t_j Q_{jk})(t_l Q_{lm}) \right] ds \tag{61}$$

therefore

$$\begin{aligned} \sum \frac{\partial K_{km}}{\partial U_l} U_m = & \int \left[ \frac{\partial a^n}{\partial U_l} (n_j Q_{jk})(n_l Q_{lm}) U_m + \frac{\partial a^t}{\partial U_l} (t_j Q_{jk})(t_l Q_{lm}) U_m \right] ds \\ & \int \left[ \frac{\partial a^n}{\partial U_l} (n_j Q_{jk}) u^n + \frac{\partial a^t}{\partial U_l} (t_j Q_{jk}) u^t \right] ds \end{aligned} \tag{62}$$

$$\frac{\partial f_k}{\partial U_l} = \int \left[ \frac{\partial a^n}{\partial U_l} (n_j Q_{jk})(h - h_0) + \frac{\partial a^t}{\partial U_l} (t_j Q_{jk})(u^s) \right] ds. \tag{63}$$

There upon  $\frac{\partial a^n}{\partial U_l}$  and  $\frac{\partial a^t}{\partial U_l}$  can be derived as

$$\frac{\partial a^n}{\partial U_l} = \frac{\partial a^n}{\partial u^n} \frac{\partial u^n}{\partial U_l} + \frac{\partial a^n}{\partial u^t} \frac{\partial u^t}{\partial U_l} \tag{64}$$

$$\frac{\partial a^t}{\partial U_l} = \frac{\partial a^t}{\partial u^n} \frac{\partial u^n}{\partial U_l} + \frac{\partial a^t}{\partial u^t} \frac{\partial u^t}{\partial U_l}. \tag{65}$$

Furthermore by expanding all the terms in the two equations above

$$\begin{aligned} \frac{\partial a^n}{\partial u^n} = & \left[ -\frac{\Gamma_n}{\delta n^3} \right] \left[ \left(1 - \alpha\right) \left(1 - \frac{\Delta n}{\delta n}\right)^{\alpha-2} \left(\frac{m}{\alpha} + \frac{\Delta n}{\delta n}\right)^{m-1} + (m - 1) \left(1 - \frac{\Delta n}{\delta n}\right)^{\alpha-1} \left(\frac{m}{\alpha} + \frac{\Delta n}{\delta n}\right)^{m-2} \right] (m + \alpha) \\ & \times \left[ \Gamma_t \left(1 - \frac{|\Delta t|}{\delta t}\right)^\beta \left(\frac{n}{\beta} + \frac{|\Delta t|}{\delta t}\right)^n + \langle \phi_t - \phi_n \rangle \right] \end{aligned} \tag{66}$$

$$\frac{\partial a^n}{\partial u^t} = \frac{\Gamma_n}{\delta n^2} \frac{\Gamma_t}{\delta t} \left[ \left(1 - \frac{\Delta n}{\delta n}\right)^{\alpha-1} \left(\frac{m}{\alpha} + \frac{\Delta n}{\delta n}\right)^{m-1} \right] (m + \alpha) \times \left[ \beta \left(1 - \frac{|\Delta t|}{\delta t}\right)^{\beta-1} \left(\frac{n}{\beta} + \frac{|\Delta t|}{\delta t}\right)^n - n \left(1 - \frac{|\Delta t|}{\delta t}\right)^\beta \left(\frac{n}{\beta} + \frac{|\Delta t|}{\delta t}\right)^{n-1} \right] \times \frac{|\Delta t|}{\Delta t} \tag{67}$$

$$\frac{\partial a^t}{\partial u^n} = \frac{\Gamma_t}{\delta t^2} \frac{\Gamma_n}{\delta n} \left[ \left(1 - \frac{|\Delta t|}{\delta t}\right)^{\beta-1} \left(\frac{n}{\beta} + \frac{|\Delta t|}{\delta t}\right)^{n-1} \right] (n + \beta) \times \left[ \alpha \left(1 - \frac{\Delta n}{\delta n}\right)^{\alpha-1} \left(\frac{m}{\alpha} + \frac{\Delta n}{\delta n}\right)^m - m \left(1 - \frac{\Delta n}{\delta n}\right)^\alpha \left(\frac{m}{\alpha} + \frac{\Delta n}{\delta n}\right)^{m-1} \right] \tag{68}$$

$$\begin{aligned} \frac{\partial a^t}{\partial u^t} = & \left[ -\frac{\Gamma_t}{\delta t^3} \right] \left[ \left(1 - \beta\right) \left(1 - \frac{|\Delta t|}{\delta t}\right)^{\beta-2} \left(\frac{n}{\beta} + \frac{|\Delta t|}{\delta t}\right)^{n-1} + (n - 1) \left(1 - \frac{|\Delta t|}{\delta t}\right)^{\beta-1} \left(\frac{n}{\beta} + \frac{|\Delta t|}{\delta t}\right)^{n-2} \right] (n + \beta) \\ & \times \left[ \Gamma_n \left(1 - \frac{\Delta n}{\delta n}\right)^\alpha \left(\frac{m}{\alpha} + \frac{\Delta n}{\delta n}\right)^m + \langle \phi_n - \phi_t \rangle \right] \times \frac{|\Delta t|}{\Delta t} \end{aligned} \tag{69}$$

and

$$\frac{\partial u^n}{\partial U_l} = n_l Q_{lL} \quad \text{and} \quad \frac{\partial u^t}{\partial U_l} = t_l Q_{lL}. \tag{70}$$

By substituting Eqs. (66)–(69) into Eq. (62) and Eq. (63) the stiffness matrix is

$$T_{kl} = \int (n_j Q_{jk}) \left( a^n (n_l Q_{lL}) + \left( \frac{\partial a^n}{\partial u^n} n_l Q_{lL} (u^n - (h - h_0)) \right) + \left( \frac{\partial a^n}{\partial u^t} t_l Q_{lL} (u^n - (h - h_0)) \right) \right) ds + (t_j Q_{jk}) \tag{71}$$

$$\begin{aligned} & \left( a^t (t_l Q_{ll}) + \left( \frac{\partial a^t}{\partial u^t} t_l Q_{ll} (u^t - (h - h_0)) \right) + \left( \frac{\partial a^n}{\partial u^n} t_l Q_{ll} (u^n - (h - h_0)) \right) \right) ds \\ & = \int (a^{NN} (n_j Q_{jk}) (n_l Q_{ll}) + a^{NT} (n_j Q_{jk}) (t_l Q_{ll}) + a^{TN} (t_j Q_{jk}) (n_l Q_{ll}) + a^{TT} (t_j Q_{jk}) (t_l Q_{ll})) ds. \end{aligned} \tag{72}$$

and

$$a^{NN} = \left[ a^n + \frac{\partial a^n}{\partial u^n} (u^n - (h - h_0)) \right]$$

$$a^{NT} = \frac{\partial a^n}{\partial u^t} (u^n - (h - h_0))$$

$$a^{TN} = \frac{\partial a^t}{\partial u^n} (u^t - u^s)$$

$$a^{TT} = \left[ a^t + \frac{\partial a^t}{\partial u^t} (u^t - u^s) \right].$$

And the residual (RHS) is expressed as

$$\begin{aligned} n_k = & K_{kl} U_l - f_k = \\ & \int [a^n (n_j Q_{jk}) (n_l Q_{ll}) U_l + a^t (t_j Q_{jk}) (t_l Q_{ll}) U_l] ds \\ & \int [a^n (h - h_0) (n_j Q_{jk}) + a^t u^s (t_j Q_{jk})] ds = \\ & \int [a^n (n_j Q_{jk}) (u^n - (h - h_0)) + a^t (t_j Q_{jk}) (u^t - u^s)]. \end{aligned} \tag{73}$$

### Appendix 2

To find the stiffness matrix for the diffusion flux it is necessary to define the weak form of Eq. 8

$$\int_{S_T} \left( j_{gb} - h \mathcal{D}_{gb} \frac{\partial \sigma^n}{\partial s} \right) \delta j_{gb} ds = 0 \tag{74}$$

where  $\delta j_{gb}$  is a “kinematically” admissible atomic flux-field,  $h$  represents diffusion zone thickness,  $\delta_{gb}$ , therefore

$$\int_{S_T} j_{gb} \delta j_{gb} ds = \int_{S_T} \left( h \mathcal{D}_{gb} \frac{\partial \sigma^n}{\partial s} \right) \delta j_{gb} ds. \tag{75}$$

By applying the divergence theorem to the Eq. (75) there results

$$\int_{S_T} j_{gb} (\delta j_{gb}) ds = - \int_{S_T} \sigma^n \frac{\partial (h \mathcal{D}_{gb} \delta j_{gb})}{\partial s} ds + [h \mathcal{D}_{gb} \sigma^n (\delta j_{gb})]_+^+ = - \int_{S_T} \sigma^n \mathcal{D}_{gb} h \frac{\partial (\delta j_{gb})}{\partial s} ds - \int_{S_T} \sigma^n \mathcal{D}_{gb} \frac{\partial h}{\partial s} \delta j_{gb} ds + [\sigma^n \mathcal{D}_{gb} h (\delta j_{gb})]_+^+ \tag{76}$$

The diffusion zone thickness,  $h$ , at any time between two iterations can be defined as  $h = h(t)(1 - \alpha) + h(t + \Delta t)\alpha$ , where  $0 \leq \alpha \leq 1$  is an adjustable parameter controlling the integration scheme and  $h(t)$  and  $h(t + \Delta t)$  are related as  $h(t + \Delta t) = h(t) + \Delta h$ . By substituting this relation between  $h(t)$  and  $h(t + \Delta t)$  the thickness is obtained as

$$h = h(t) + \Delta h \alpha \tag{77}$$

where  $h(t)$  is  $h$  at time  $t$ , shown hereafter as  $h_0$ . By setting  $\alpha = 0$  the integration formula is reduced to the standard explicit forward-Euler scheme, whereas  $\alpha = 1$  represents the first iteration in a fully implicit integration scheme. In this work, we have set  $\alpha = 0.5$  to represent the average  $h$  between each two iterations. By substituting Eq. (77) to Eq. (76) and recalling  $\Delta h = \Delta t \left( -\Omega \frac{\partial j_{gb}}{\partial s} \right)$ , we find

$$\int_{S_T} \left( j_{gb} (\delta j_{gb}) - \sigma^n \mathcal{D}_{gb} \alpha \Omega \Delta t \frac{\partial j_{gb}}{\partial s} \frac{\partial (\delta j_{gb})}{\partial s} - \sigma^n \mathcal{D}_{gb} \alpha \Omega \Delta t \frac{\partial^2 j_{gb}}{\partial s^2} \delta j_{gb} \right) ds = - \int_{S_T} \left( \sigma^n \mathcal{D}_{gb} h_0 \frac{\partial (\delta j_{gb})}{\partial s} + \sigma^n \mathcal{D}_b \frac{\partial h_0}{\partial s} \delta j_{gb} \right) ds + [\sigma^n \mathcal{D}_{gb} h (\delta j_{gb})]_+^+ \tag{78}$$

This term is used to calculate the residual vector required to define the element in subroutine UEL. The output of the weak form formulation represents the value for diffusion flux at each node. The first derivative of the flux with respect to position  $s$  is used to find the change in grain boundary thickness. In our simulation the diffusion zone element between two grains is defined as a 2-node one-dimensional element with two Gaussian points in a Lagrange framework (cf. Fig. 8). The shape functions are linear over the element and are defined as

$$S_1 = \frac{1}{2}(1 - \xi)$$

$$S_2 = \frac{1}{2}(1 + \xi)$$

which preserve the continuity of the diffusion flux field variable,  $J$ , but not its first derivative which represents the change in grain boundary thickness and is constant over each element. Therefore at the node shared between two adjacent diffusion zone elements, the average value of the derivative of diffusion flux between two elements is used to calculate incremental change in grain boundary thickness.

Eq. (75) and Eq. (76) can be expressed respectively as

$$\begin{aligned} & \int_{S_\Gamma} \left( \delta j_{(gb)k} S_{kl} S_{mn} - \mathcal{D}_{gb} \alpha \Omega \sigma^n \Delta t \delta j_{(gb)k} \frac{\partial S_{kl}}{\partial \zeta} \frac{\partial S_{mn}}{\partial \zeta} \left( \frac{2}{l} \right)^2 - \mathcal{D}_{gb} \alpha \Omega \sigma^n \Delta t \delta j_{(gb)k} S_{kl} \frac{\partial^2 S_{mn}}{\partial \zeta^2} \left( \frac{2}{l} \right)^2 \right) d\zeta \left( \frac{l}{2} \right) \\ & = - \int \mathcal{D}_{gb} \Omega \sigma^n h_0 \delta j_{(gb)k} \frac{\partial S_{kl}}{\partial \zeta} d\zeta + \mathcal{D}_{gb} \Omega \sigma^n \frac{\partial h_0}{\partial \zeta} \delta j_{(gb)k} S_{kl} + [h \mathcal{D}_{gb} \sigma^n (S_{kl} \delta j_{(gb)k})]_+^+ \end{aligned} \tag{79}$$

where  $\sigma^n$  is calculated from the cohesive traction-separation equation inside the grain boundary. Over each element,  $\sigma^n$  is determined as a function of traction on each element's node using linear shape function  $S$

$$\sigma^n = \sum_{K=1}^3 S_K \sigma_K.$$

Since the shape function is linear, the second derivative in Eq. (79) is zero,  $\frac{\partial^2 S}{\partial \zeta^2} = 0$ . By implementing the summation in the Eq. (79), the finite element form of the equation is obtained as

$$K_{kn} j_{(gb)n} = F_n \tag{80}$$

where

$$K_{kn} = \int_{S_\Gamma} \left( S_{kl} S_{mn} - \mathcal{D}_{gb} \alpha \Omega \sigma^n \frac{\partial S_{kl}}{\partial \zeta} \frac{\partial S_{mn}}{\partial \zeta} \left( \frac{2}{l} \right)^2 \right) d\zeta \left( \frac{l}{2} \right) \tag{81}$$

and

$$F_n = - \int \left( \mathcal{D}_{gb} \sigma^n h_0 \frac{\partial S_{kl}}{\partial \zeta} + \mathcal{D}_{gb} \sigma^n \frac{\partial h_0}{\partial \zeta} S_{kl} \right) d\zeta + [h \mathcal{D}_{gb} \sigma^n (S_{kl} \delta j_k)]_+^+.$$

### Appendix 3

To compute the change in the shape of the void, Eq. (41) needs to be integrated with respect to time. The value of  $\phi$  and its derivative is negligible compared to the other parameters and can be eliminated from the equation. The term that represents the curvature of the void surface in the flux equation is integrated using a semi-implicit Euler scheme where  $\Delta h(s)$  denotes the normal displacement of the void surface in the reference configuration during time interval  $\Delta t$ , so  $\Delta h = \Delta t v_n(t)$ ,

Let  $\kappa_0$  denote the curvature of the surface at time  $t$ . Then, the curvature at time  $t + \Delta t$  may be estimated as

$$\kappa(t + \Delta t) = \kappa_0 + \frac{\partial^2 \Delta h}{\partial s^2} + \kappa_0^2 \Delta h + \mathcal{O}(\Delta h^2). \tag{82}$$

At any time between  $t$  and  $t + \Delta t$  the curvature is approximated as

$$\kappa = (1 - \alpha) \kappa_0 + \alpha \kappa(t + \Delta t) \tag{83}$$

where  $0 \leq \alpha \leq 1$ , similar to grain boundary diffusion zone, is an adjustable parameter to control the integration scheme. Finally, substituting Eq. (82) to Eq. (41) we obtain the final weak form for surface diffusion zone as

$$\int_{\Gamma} j_s \delta j_s - \alpha \Delta t \mathcal{D}_s \gamma_s \Omega \left( \frac{\partial^3 j_s}{\partial s^3} + \kappa_0^2 \frac{\partial j_s}{\partial s} \right) \frac{\partial \delta j_s}{\partial s} ds = - \int_{\Gamma} \mathcal{D}_s (\gamma_s \kappa_0) \frac{\partial \delta j_s}{\partial s} ds + [\mathcal{D}_s (\gamma_s \kappa_0) (\delta j_s)]_+^+ \tag{84}$$

After evaluating surface diffusion at each node, we compute the normal displacement from  $\Delta h = -\Delta t \Omega \delta j_s / \partial s$ .

### References

Barenblatt, G.I., 1959. The formation of equilibrium cracks during brittle fracture. general ideas and hypotheses. axially-symmetric cracks. *J. Appl. Math. Mech.* 23 (3), 622–636.

Bringa, E.M., Traiviratana, S., Meyers, M.A., 2010. Void initiation in fcc metals: effect of loading orientation and nanocrystalline effects. *Acta Mater.* 58 (13), 4458–4477.

Conrad, H., Narayan, J., 5 2000. On the grain size softening in nanocrystalline materials. *Scripta Mater.* 42 (11), 1s025–1030.

ABAQUS (2013). Dassault Systèmes, Providence, RI, USA ABAQUS Documentation.

- Dongare, A.M., Rajendran, A.M., LaMattina, B., Zikry, M.A., Brenner, D.W., Sep 2009. Atomic scale simulations of ductile failure micromechanisms in nanocrystalline Cu at high strain rates. *Phys. Rev. B* 80, 104108.
- Dugdale, D.S., 1960. Yielding of steel sheets containing slits. *J. Mech. Phys. Solid.* 8 (2), 100–104.
- Falk, M.L., Needleman, A., Rice, J.R., 3 2001. A critical evaluation of dynamic fracture simulations using cohesive surface. *J. Phys. IV* 11, 43–50.
- Fish, J., Belytschko, T., 2007. *A First Course in Finite Elements*. JohnWiley and Sons.
- Fu, H.H., Benson, D.J., Meyers, M.A., 2001. Analytical and computational description of effect of grain size on yield stress of metals. *Acta Mater.* 49 (13), 2567–2582.
- Ghazi, N., Kysar, J.W., 2016. Experimental investigation of plastic strain recovery and creep in nanocrystalline copper thin films. *Exp. Mech.* 1–12.
- Gibbs, J.W., 1902. *Elementary principles in statistical mechanics : developed with especial reference to the rational foundation of thermodynamics*. Charles Scribner's sons.
- Gleiter, H., 2000. Nanostructured materials: basic concepts and microstructure. *Acta Mater.* 48 (1), 1–29.
- Hahn, E.N., Meyers, M.A., 2015. Grain-size dependent mechanical behavior of nanocrystalline metals. *Mater. Sci. Eng., A* 646 (Suppl. C), 101–134.
- Harper, J.M.E., Cabral, C., Andricacos, P.C., Gignac, L., Noyan, I.C., Rodbell, K.P., Hu, C.K., 1999. Mechanisms for microstructure evolution in electroplated copper thin films near room temperature. *J. Appl. Phys.* 86 (5), 2516–2525.
- Herring, C., Kingston, W., 1951. *The Physics of Powder Metallurgy*, vol. 143 MacGraw-Hill, New York.
- Hugo, R.C., Kung, H., Weertman, J.R., Mitra, R., Knapp, J.A., Follstaedt, D.M., 2003. In-situ tem tensile testing of dc magnetron sputtered and pulsed laser deposited ni thin films. *Acta Mater.* 51, 1937–1943.
- International A. Metals Handbook. ASM International, Materials Park, Ohio.
- Kanninen, M.F., Popelar, C.H., 1985. *Advanced Fracture Mechanics*. Oxford Science Publication, New York.
- Koch, R., 2010. Stress in evaporated and sputtered thin films – a comparison. *Surf. Coating. Technol.* 204 (12), 1973–1982.
- Koslowski, M., AUG 17 2010. Effect of grain size distribution on plastic strain recovery. *Phys. Rev. B* 82 (5).
- Kumar, K.S., Swygenhoven, H.V., Suresh, S., 2003a. Mechanical behavior of nanocrystalline metals and alloys. *Acta Mater.* 51 (19), 5743–5774 *The Golden Jubilee Issue. Selected topics in Materials Science and Engineering: Past, Present and Future*.
- Kumar, K.S., Suresh, S., Chisholm, M.F., Horton, J.A., Wang, P., 2003b. Deformation of electrodeposited nanocrystalline nickel. *Acta Mater.* 51 (2), 387–405.
- Li, X., Bower, A.F., Suo, Z., Shih, C.F., 1997. A finite element analysis of the motion and evolution of voids due to strain and electromigration induced surface diffusion. *J. Mech. Phys. Solid.* 45 (9), 1473–1493.
- Li, X., Wei, Y., Yang, W., Gao, H., SEP 22 2009. Competing grain-boundary- and dislocation-mediated mechanisms in plastic strain recovery in nanocrystalline aluminum. *Proc. Natl. Acad. Sci. U. S. A.* 106 (38), 16108–16113.
- Meyers, M.A., Mishra, A., Benson, D.J., 2006. Mechanical properties of nanocrystalline materials. *Prog. Mater. Sci.* 51 (4), 427–556.
- Needleman, A., 09 1987Needleman. A continuum model for void nucleation by inclusion debonding. *J. Appl. Mech.* 54 (3), 525–531.
- Needleman, A., 1990. An analysis of tensile decohesion along an interface. *J. Mech. Phys. Solid.* 38 (3), 289–324.
- Park, K., Paulino, G.H., Roesler, J.R., 2009. A unified potential-based cohesive model of mixed-mode fracture. *J. Mech. Phys. Solid.* 57 (6), 891–908.
- Péron-Lühns, V., Jérusalem, A., Sansoz, F., Stainier, L., Noels, L., 2013. A two-scale model predicting the mechanical behavior of nanocrystalline solids. *J. Mech. Phys. Solid.* 61 (9), 1895–1914.
- Petegem, S.V., Torre, F.D., Segers, D., Swygenhoven, H.V., 2003. Free volume in nanostructured ni. *Scripta Mater.* 48 (1), 17–22.
- Peterson, P.E., Hillerborg, A., Modeer, M., 1976. Analysis of crack formation and crack growth in concrete by means of fracture mechanics and finite elements. *Cement Concr. Res.* 6, 773–782.
- Prandtl, L., 1933. Ein gedankenmodell für den zerreißvorgang sproder körper. *Zeitschrift für angewandte Mathematik undMechanik* 13, 129–133.
- Rajagopalan, J., Han, J.H., Saif, M.T.A., 2007. Plastic deformation recovery in freestanding nanocrystalline aluminum and gold thin films. *Science* 315 (5820), 1831–1834.
- Rajagopalan, J., Han, J.H., Salf, M.T.A., NOV 2008. On plastic strain recovery in freestanding nanocrystalline metal thin films. *Scripta Mater.* 59 (9), 921–926.
- Rudd, R.E., 06 2009. Article void growth in bcc metals simulated with molecular dynamics using the finnis-sinclair potential. 89.
- Schiotz, J., Di Tolla, F.D., Jacobsen, K.W., 02 1998. Softening of nanocrystalline metals at very small grain sizes. *Nature* 391 (6667), 561–563.
- Shet, C., Chandra, N., September 2002. Analysis of energy balance when using cohesive zone models to simulate fracture processes. *J. Eng. Mater. Technol.* 124 (4), 440–450.
- Spolenak, R., Volkert, C.A., Ziegler, S., Panofen, C., Brown, W.L., 2001. Reverse stress relaxation in Cu thin films. *Mater. Res. Soc. Symp. Proc.* 673 (141–6).
- Stroud, K.A., 2003. *Advanced Engineering Mathematics*. Palgrave, fourth ed. .
- Swygenhoven, H.V., Derlet, P.M., 2001. Grain-boundary sliding in nanocrystalline fcc metals. *Phys. Rev. B* 64 (9), 224105.
- Swygenhoven, H.V., Weertman, J.R., 2006. Deformation in nanocrystalline metals. *Mater. Today* 9 (5), 24–31.
- Swygenhoven, H.V., Derlet, P.M., Frøseth, A.G., 2006. Nucleation and propagation of dislocations in nanocrystalline fcc metals. *Acta Mater.* 54 (7), 1975–1983.
- Takahashi, Y., Takahashi, K., Nishiguchi, K., 1991. A numerical analysis of void shrinkage processes controlled by coupled surface and interface diffusion. *Acta Metall. Mater.* 39 (12), 3199–3216.
- Thornton, J.A., Hoffman, D.W., 1989. Stress-related effects in thin films. *Thin Solid Films* 171, 5–31.
- Thouless, M.D., 1993. Effect of surface diffusion on the creep of thin films and sintered arrays of particles. *Acta Metall. Mater.* 41 (4), 1057–1064.
- Van Swygenhoven, H., Derlet, P.M., Hasnaoui, A., 2002. Atomic mechanism for dislocation emission from nanosized grain boundaries. *Phys. Rev. B* 66 (8), 024101.
- Vlassak, J.J., Nix, W.D., 12 1992. A new bulge test technique for the determination of young's modulus and Poisson's ratio of thin films. *J. Mater. Res.* 7, 3242–3249.
- Weertman, J.R., 2007. *Nanostructured Materials: Processing, Properties and Applications*, second ed. William Andrew Inc, NY page 537.
- Wei, Y.J., Anand, L., 2004. Grain-boundary sliding and separation in polycrystalline metals: application to nanocrystalline fcc metals. *J. Mech. Phys. Solid.* 52 (11), 2587–2616.
- Wei, Q., Cheng, S., Ramesh, K.T., Ma, E., 2004. Effect of nanocrystalline and ultrafine grain sizes on the strain rate sensitivity and activation volume: fcc versus bcc metals. *Mater. Sci. Eng., A* 381, 71–79.
- Wei, Y., Su, C., Anand, L., 2006. A computational study of the mechanical behavior of nanocrystalline fcc metals. *Acta Mater.* 54 (12), 3177–3190.
- Wei, X., Lee, D., Shim, S., Chen, X., Kysar, J.W., 2007. Plane-strain bulge test for nanocrystalline copper thin films. *Scripta Mater.* 57 (6), 541–544.
- Wei, Y., Bower, A.F., Gao, H., 2008a. Recoverable creep deformation and transient local stress concentration due to heterogeneous grain-boundary diffusion and sliding in polycrystalline solids. *J. Mech. Phys. Solid.* 56 (4), 1460–1483.
- Wei, Y., Bower, A.F., Gao, H., 2008b. Enhanced strain-rate sensitivity in fcc nanocrystals due to grain-boundary diffusion and sliding. *Acta Mater.* 56 (8), 1741–1752.
- Wei, X., Kysar, J.W., 2011. Residual plastic strain recovery driven by grain boundary diffusion in nanocrystalline thin films. *Acta Mater.* 59 (10), 3937–3945.
- Wolf, D., Yamakov, V., Phillpot, S.R., Mukherjee, A.K., 2003. Deformation mechanism and inverse hall-petch behavior in nanocrystalline materials. *Z. Metallkd.* 94 (10), 1091–1097 2015/04/27.
- Wolf, D., Yamakov, V., Phillpot, S.R., Mukherjee, A., Gleiter, H., 2005. Deformation of nanocrystalline materials by molecular-dynamics simulation: relationship to experiments? *Acta Mater.* 53 (1), 1–40.
- Xiang, Y., Tsui, T.Y., Vlassak, J.J., 6 2006. The mechanical properties of freestanding electroplated Cu thin films. *J. Mater. Res.* 21, 1607–1618.
- Xie, Y., Koslowski, M., JUN 2016. Inelastic recovery in nano and ultrafine grained materials. *Model. Simulat. Mater. Sci. Eng.* 24 (5).
- Xu, X.P., Needleman, A., 1993. Void nucleation by inclusion debonding in a crystal matrix. *Model. Simulat. Mater. Sci. Eng.* 1 (2), 111.
- Yilmaz, M., Kysar, J.W., 2013. Monolithic integration of nanoscale tensile specimens and mems structures. *Nanotechnology* 24 (16).
- Zienkiewicz, O.C., Taylor, R.L., 2005. *The Finite Element Method for Solid and Structural Mechanics*. Elsevier Butterworth-Heinemannsterdam, Amsterdam; Boston.